

# 10

## Induced interaction

As discussed in the last section of Chapter 9 a pair of nucleons can interact with each other through the nuclear surface in a process in which one nucleon excites a vibrational mode which is then absorbed by the other nucleon (see inset Fig. 10.1). This process leads to a renormalization of the nucleon–nucleon interaction which, for nucleons close to the Fermi energy, is controlled by the exchange of low-lying surface collective vibrations. This is because low-energy surface vibrations match the frequencies of these nucleons and are very collective. This argument is the same as that used to explain the central role of surface vibrations in renormalizing the single-particle motion. The contribution of surface vibrations to the single-particle self-energy and to the  $\omega$ -mass was analysed in Chapter 9 and a simplified version of the particle-vibration coupling model was introduced in Section 9.3. It gave explicit expressions for both the  $\omega$ -mass and the induced pairing interaction and pairing gap due to phonon exchange. They both have a simple dependence on the coupling strength  $g_{p-v}$  which is defined in equation (9.31). The present chapter extends the discussion of the induced interaction and presents the results of microscopic calculations. Section 10.3 presents results in a slab model, where the simplicity of the infinite system is retained (absence of shell structure), without losing surface effects.

### 10.1 Simple estimates

Estimates of the induced pairing interaction due to phonon exchange were obtained in Section 9.3 in a model with constant matrix elements and a uniform distribution of single-particle levels. The present section extends that discussion by including shell effects (Broglia *et al.* (2001)). The starting point is a perturbation expression for the induced interaction written in terms of  $(j, j)$  coupled

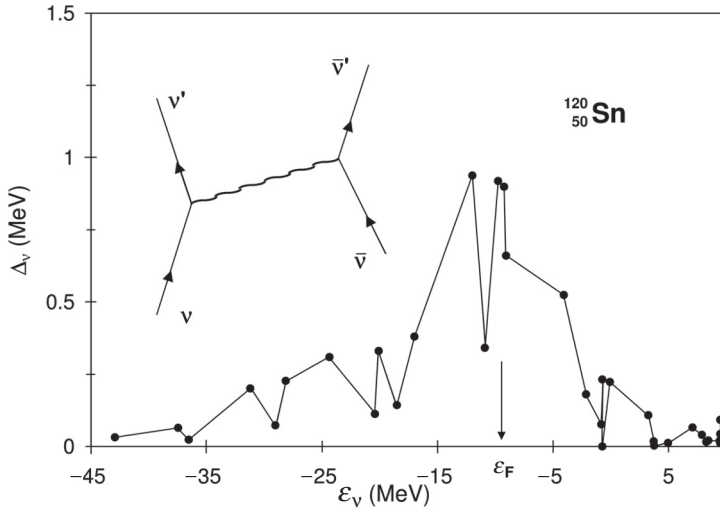


Figure 10.1. State-dependent pairing gap  $\Delta_v$  for the nucleus  $^{120}\text{Sn}$ , calculated by making use of the induced interaction (see inset, where particles are represented by arrowed lines and phonons by a wavy line) (after Barranco *et al.* (1999)). Reprinted with permission from Barranco *et al.*, *Phys. Rev. Lett.* **83**: 2147–50 (1999). Copyright 1999 the American Physical Society.

matrix elements

$$v_{jj'} \equiv \langle (jj)_0 | v | (j'j')_0 \rangle = \sum_{\lambda} v_{jj'}^{\lambda}, \quad (10.1)$$

where

$$v_{jj'}^{\lambda} = \frac{2}{\sqrt{(2j+1)(2j'+1)}} \frac{V^2(j, j'; \lambda)}{D_{\lambda}}. \quad (10.2)$$

Here  $v_{jj'}$  is the induced matrix element for scattering of a pair of nucleons from the state  $j$  with energy  $\varepsilon_j$  to the state  $j'$  with energy  $\varepsilon_{j'}$ . The nucleons are coupled to a total angular momentum zero in both the initial and final states (see Appendix D, equations (D.11)–(D.14)). The matrix element  $v_{jj'}$  is a sum of components  $v_{jj'}^{\lambda}$  corresponding to the exchange of phonons with different multiplicities  $\lambda$  and energies  $\hbar\omega_{\lambda}$ . The  $V^2(j, j'; \lambda)$  are the square of particle-vibration coupling matrix elements

$$V^2(j, j', \lambda) = \frac{\beta_{\lambda}^2}{2\lambda + 1} \langle j' | R_0 \frac{\partial U}{\partial r} | j \rangle^2 \langle l' j' || Y_{\lambda} || l j \rangle^2, \quad (10.3)$$

introduced in Section 8.3 and defined in Appendix D (equation (D.9)). They were used in equation (9.6) for the calculation of single-particle self-energies. The quantity  $\beta_{\lambda}$  is the root mean square fluctuation of the collective coordinate

of the phonon of multipolarity  $\lambda$  in the ground state and  $\langle j'|R_0\partial U/\partial\lambda|j\rangle$  is a radial coupling matrix element. The energy denominator  $D_\lambda$  in equation (10.2) can be approximated in different ways. In Section 9.3 (equation (9.34)) it was written as

$$\frac{1}{D_\lambda} \approx \frac{\hbar\omega_\lambda}{(\varepsilon_i - \varepsilon_j)^2 - (\hbar\omega_\lambda)^2},$$

which reduces to  $D_\lambda \approx -\hbar\omega_\lambda$  when  $\varepsilon_i = \varepsilon_j$ . The microscopic calculations presented in the next section use a more accurate energy denominator from Bloch–Horowitz perturbation theory (Bloch and Horowitz (1958))

$$D_\lambda = E_0 - (\hbar\omega_\lambda + e_j + e_{j'}), \quad (10.4)$$

used in Barranco *et al.* (1999) for calculating the contribution of phonon exchange to pairing in nuclei. Here  $e_j = |\varepsilon_j - \varepsilon_F|$  are single-particle energies measured from the Fermi energy and  $E_0$  is a (negative) BCS correlation energy.

The diagonal ( $j = j'$ ) induced matrix elements can be estimated from

$$\begin{aligned} v_{jj}^\lambda &= -\frac{2\beta_\lambda^2}{2\lambda + 1} \frac{\langle j|R_0\frac{\partial U}{\partial r}|j\rangle^2}{(2j + 1)} \frac{\langle j||Y_\lambda||j\rangle^2}{\hbar\omega_\lambda} \\ &\approx -\frac{0.2\beta_\lambda^2}{2\lambda + 1} \frac{(50 \text{ MeV})^2}{\hbar\omega_\lambda}, \end{aligned} \quad (10.5)$$

with the approximations  $D_\lambda \approx -\hbar\omega_\lambda$  for the energy denominator and  $\langle j||Y_\lambda||j\rangle^2 \approx 0.1(2j + 1)$  for the square of the reduced matrix element, as well as  $\langle j|R_0\partial U/\partial r|j\rangle \approx -50 \text{ MeV}$  (Appendix D). Only even values of  $\lambda$  contribute when  $j = j'$  because of the parity selection rule contained in the reduced matrix elements  $\langle j||Y_\lambda||j\rangle$ . There is also an angular momentum constraint  $\lambda \leq 2j$ . For  $^{120}\text{Sn}$ ,  $\beta_2 = 0.119$  and  $\hbar\omega_2 = 1.171 \text{ MeV}$  (Beer *et al.* (1970)), while an RPA estimate of the corresponding parameters for  $\lambda = 4$  leads to  $\beta_4 = 0.07$  and  $\hbar\omega_4 = 1.2 \text{ MeV}$  (Gori (2002)). Making use of these values one obtains

$$v_{jj}^2 = -1.2 \text{ MeV}, \quad v_{jj}^4 = -0.2 \text{ MeV}, \quad v_{jj} = -1.4 \text{ MeV}, \quad (10.6)$$

a number which is also consistent with the result given in equation (9.8) (note the difference of a factor of 2 between self-energy and induced interaction; see equations (9.6) and (9.35) respectively). The same factor occurs in equations (10.2) and (10.5). It has its origin in the two possible time orderings in the phonon exchange diagram shown in Fig. 8.3(c) (see inset to Fig. 10.1).

The (typical) matrix element  $v_{jj} = \langle (jj)_0|v|(j'j')_0\rangle (= -1.4 \text{ MeV})$  induced interaction reported in equation (10.6) is found to be of the same order of magnitude or even larger than the (attractive) bare interaction matrix elements reported in Fig. 8.5 (i.e.  $-1.8 \lesssim \langle j^2(0)|v_{14}|j^2(0)\rangle \leq 0$ ,  $j = s_{1/2}, p_{3/2}, d_{5/2}$ ). The fact that ‘The polarization interaction resulting from the coupling to the low frequency

modes may be considerably larger than the bare force ...' was discussed by Bohr and Mottelson (1975) in Section 6-5f p.432 (see also Broglia, Paar and Bes (1971a,b)).

Let us compare the induced interaction with the strength of the typical pairing force with constant matrix elements  $G (\approx 25/A \text{ MeV})$  tailored to reproduce the empirical value of the pairing gap  $\Delta \approx 12/\sqrt{A} \text{ MeV}$ . The pairing strength  $G$  is a matrix element between uncoupled pair states and to make the comparison the states  $|(jj)_0\rangle$  with total angular momentum zero have to be written in terms of uncoupled  $m$ -states

$$|(jj)_0\rangle = \sum_m \frac{(-1)^{j-m}}{\sqrt{2j+1}} |jm, j-m\rangle = \sum_m \frac{1}{\sqrt{(2j+1)}} |jm, \tilde{j}m\rangle,$$

where  $|\tilde{j}m\rangle$  is the time reverse of the state  $|jm\rangle$ . The expression for the matrix element  $v_{jj'}$  becomes

$$v_{jj'} = \langle (jj)_0 | v | (j'j')_0 \rangle = \sum_{mm'} \frac{1}{\sqrt{(2j'+1)(2j+1)}} \langle jm, \tilde{j}m | v | j'm', \tilde{j}'m' \rangle.$$

Assuming that the matrix elements in the  $m$ -scheme are all equal, an induced pairing interaction strength can be defined by

$$G_{\text{ind}} = -\overline{\langle jm, \tilde{j}m | v | j'm', \tilde{j}'m' \rangle},$$

and one obtains (cf. equation (D.15))

$$\overline{\langle (jj)_0 | v | (j'j')_0 \rangle} = -\frac{\sqrt{(2j+1)(2j'+1)}}{2} G_{\text{ind}}. \quad (10.7)$$

Consequently, for  $j = j'$ ,

$$G_{\text{ind}} = -\frac{2v_{jj}}{(2j+1)}. \quad (10.8)$$

The single neutron states near to the Fermi energy in  $^{120}\text{Sn}$  are  $d_{5/2}$ ,  $h_{11/2}$ ,  $s_{1/2}$ ,  $g_{7/2}$  and  $d_{5/2}$ , corresponding to an average  $\bar{j} = 7/2$ . Making use of this value, the relation (10.8) and the estimate given in equation (10.6) one obtains  $G_{\text{ind}} = 0.35 \text{ MeV}$ . This number should be compared with the empirical pairing strength  $G = (25/A) \approx 0.21 \text{ MeV}$ . In spite of the over-simplifications of this estimate it surely indicates that the induced pairing interaction due to particle-phonon coupling can account for a significant fraction of the total pairing interaction.

The estimates of  $\beta_\lambda$  and  $\hbar\omega_\lambda$  in Section 7.1 have a simple  $A$ -dependence ( $\beta_\lambda \propto A^{-2/3}$  and  $\hbar\omega_\lambda \propto A^{-2/3}$ ). Thus the matrix element

$$v_{jj}^\lambda \approx -\frac{185 \text{ MeV}}{(\lambda-1)(\lambda+2)} \frac{(1+0.001A)}{A^{2/3}} \quad (10.9)$$

is approximately independent of  $j$ . The  $A$ -dependence of the induced pairing interaction strength given in equation (10.8) can be estimated by using this relation and the average degeneracy  $(2j + 1)$  of a  $j$ -orbit near the Fermi level. This quantity can be calculated in terms of the mean value  $\bar{k}_F = (2/3)k_F$  of the Fermi momentum ( $k_F = 1.36 \text{ fm}^{-1}$ ) and of the nuclear radius  $R = 1.2A^{1/3} \text{ fm}$  ( $j \approx \bar{k}_F R$ ) leading to  $(2j + 1) \approx 2.2A^{1/3}$ . Using this estimate and equations (10.1), (10.8) and (10.9) ( $\lambda = 2$  and 4) we get

$$G_{\text{ind}} \approx \frac{29}{A} \text{ MeV}. \quad (10.10)$$

This has the same  $A$ -dependence as the empirical pairing strength but is somewhat too large.

The following three sections present the results of detailed microscopic calculations of the induced interaction. The first is a self-consistent calculation of the pairing gap for the semi-magic nucleus  $^{120}\text{Sn}$  as well as for Ca and Ti isotopes and the second is for a slab-model where shell effects are suppressed. Both of these calculations use Bloch–Horowitz energy denominators (10.4) which are always larger than the value  $\hbar\omega_\lambda$  used for the estimates in this section. In Section 10.4 a calculation is presented based on the Dyson equation, which takes into account, aside from the bare nucleon–nucleon potential, the induced pairing interaction, on equal footing to the self-energy and vertex corrections. All of these microscopic theories give induced pairing strengths which are considerably smaller by a factor of about 2 than the estimate given in equation (10.10).

## 10.2 Microscopic calculations

In this section the results of a calculation of the state-dependent pairing gap associated with the induced interaction will be presented. The discussion is based on Broglia *et al.* (2001), Barranco *et al.* (1999). In the following  $\nu$  refers to the pair state  $|(j_\nu j_\nu)_0\rangle = |j_\nu^2(0)\rangle$  with total angular momentum zero and the matrix element (see Appendix D, equation (D.15))

$$G_{\nu\nu'} = -v_{\nu\nu'} = -\frac{2\langle j_\nu^2(0)|v|j_{\nu'}^2(0)\rangle}{\sqrt{(2j_\nu + 1)(2j_{\nu'} + 1)}}, \quad (10.11)$$

so that the normalization of  $G_{\nu\nu'}$  is the same as the normalization of the induced interaction in equation (10.8), and can be directly compared with the pairing coupling constant and  $G$  ( $\approx 25/A \text{ MeV}$ ) introduced in defining the BCS pairing Hamiltonian (Chapter 3).

The calculation of the matrix elements uses the perturbation method of Bloch and Horowitz (1958). The application of this method to nuclear problems is explained in Appendix B of Bes *et al.* (1976a). In the Bloch–Horowitz approach, the exchange of phonons (vibrations) is iterated to infinite order, by the

self-consistent solution of the set of coupled equations

$$G_{\nu\nu'} = - \sum_{\lambda n} \frac{4\beta_\lambda^2(n)}{(2j_\nu + 1)(2j_{\nu'} + 1)(2L + 1)} \frac{\langle j_{\nu'} | R_0 \frac{\partial U}{\partial r} | j_\nu \rangle^2 \langle j_{\nu'} || Y_\lambda || j_\nu \rangle^2}{E_0 - [e_\nu + e_{\nu'} + \hbar\omega_\lambda(n)]}, \quad (10.12)$$

with

$$E_0 = U - E_{\text{unp}}. \quad (10.13)$$

The energy  $E_0$  in equation (10.13) is the pair-correlation energy and is the difference between the ground-state energy  $U$  including pairing correlations and the unperturbed ground state energy  $E_{\text{unp}}$ . The energies  $U$  and  $E_{\text{unp}}$  are defined explicitly in the following paragraph (see also Appendix G). The sum in equation (10.12) is taken over all multiplicities  $\lambda$ . The sum over  $n$  allows for the possibility that there may be several phonons with the same multiplicity. Equation (10.12) differs from (10.2) and (10.5) in several respects. The normalization is different because of the normalization (10.11) of  $G_{\nu\nu'}$ . In Bloch–Horowitz perturbation theory the energy denominator is the difference between the final energy of the system  $E_0$  and the energy of the, unperturbed, intermediate state (see Fig. 10.1)  $e_\nu + e_{\nu'} + \hbar\omega_\lambda(n)$ . The dependence on  $E_0$  is a feature of the Bloch–Horowitz perturbation method. The  $e_\nu$  and  $e_{\nu'}$  are magnitudes of single-particle energies of the states  $\nu$  and  $\nu'$  measured from the Fermi energy. As the correlation energy  $E_0$  is negative, the denominator in the last factor in equation (10.12) is always negative and each term contributing to  $G_{\nu\nu'}$  is positive. The expression for  $G_{\nu\nu'}$  (equation (10.12)) is automatically symmetric in the initial and final states  $\nu$  and  $\nu'$ . Thus it is not necessary to make the *ad hoc* symmetrization as in equations (9.33), (9.34).

The unperturbed ground-state energy in equation (10.13) is

$$E_{\text{unp}} = \sum_{\substack{j_\nu \\ \varepsilon_\nu < \varepsilon_F}} (2j_\nu + 1)(\varepsilon_\nu - \varepsilon_F). \quad (10.14)$$

where  $\varepsilon_\nu$  are single-particle energies and  $\varepsilon_F$  is the Fermi energy. The perturbed energy is

$$U = \sum_{j_\nu} (2j_\nu + 1)(\varepsilon_\nu - \varepsilon_F) V_\nu^2 - \sum_{j_\nu j_{\nu'}} \frac{(2j_\nu + 1)(2j_{\nu'} + 1)}{4} \frac{G_{\nu\nu'} \Delta_{j_\nu} \Delta_{j_{\nu'}}}{4 E_{j_\nu} E_{j_{\nu'}}}. \quad (10.15)$$

Thus  $E_0 = U - E_{\text{unp}}$  is the ground-state correlation energy. The gap parameters  $\Delta_\nu$  satisfy the gap equation

$$\Delta_{j_\nu} = \sum_{j_{\nu'}} \frac{2j_{\nu'} + 1}{2} \frac{G_{\nu\nu'} \Delta_{j_{\nu'}}}{2E_{j_{\nu'}}}, \quad (10.16)$$

where the quasiparticle energies are given by

$$E_{j_v} = \sqrt{(\varepsilon_{j_v} - \varepsilon_F)^2 + \Delta_v^2}. \quad (10.17)$$

The BCS occupation probabilities are defined by

$$V_{j_v}^2 = \frac{1}{2} \left( 1 - \frac{\varepsilon_{j_v} - \varepsilon_F}{E_{j_v}} \right),$$

and the Fermi energy  $\varepsilon_F$  is fixed by the condition

$$N = 2 \sum_{j_v} V_{j_v}^2. \quad (10.18)$$

By using the gap equation (10.16) the second term in equation (10.15) can be written as a single sum

$$\sum_{j_v j_{v'}} \frac{(2j_v + 1)(2j_{v'} + 1)}{4} \frac{G_{vv'}}{4} \frac{\Delta_{j_v} \Delta_{j_{v'}}}{E_{j_v} E_{j_{v'}}} = \sum_{j_v} \frac{(2j_v + 1)}{2} \frac{\Delta_{j_v}^2}{2E_{j_v}} \quad (10.19)$$

The basic ingredients needed in solving these equations are the single-particle energies  $\varepsilon_v$  and the corresponding wavefunctions  $\phi_v(\vec{r})$ , as well as the phonon energies  $\hbar\omega_\lambda(n)$  and the transition probabilities

$$B(E\lambda : 0 \rightarrow \lambda(n)) = \left( \frac{3}{4\pi} Z e R^\lambda \right)^2 \beta_\lambda^2$$

of the vibrational modes. The quantities  $\varepsilon_v$  and  $\phi_v(\vec{r})$  are calculated assuming nucleons to move in an average field containing a spin-orbit term and parametrized in terms of a Saxon–Woods potential, with standard parameters. The vibrations are calculated in the quasiparticle random phase approximation (see equation (8.47)), adjusting the coupling constant to reproduce the energy and transition probabilities of lowest-lying vibrational states. The resulting values are, as a rule, quite close to the self-consistent value relating the potential variation to the density variation in a self-sustained normal mode of oscillation.

In Fig. 10.1 we show the calculated state-dependent pairing gap for the nucleus  $^{120}\text{Sn}$ . The matrix elements  $G_{vv'}$  are shown in Fig. 10.2 and Table 10.1. The corresponding state dependence of  $\Delta_v$  is closely connected with the strong state dependence of  $G_{vv'}$ . This dependence reflects the fact that scattering processes implying spin-flip are essentially possible only because of quantal fluctuations.

In any case, the average value of these matrix elements associated with states lying close to the Fermi energy is  $\bar{G} = \sum_{v \geq v'} G_{vv'} / 15 \approx 0.11 \text{ MeV}$  (see Section 9.3, discussion following equation (9.35), note that  $\bar{G}$  is to be compared to  $|\bar{v}|$ ), while the pairing-correlation energy is  $E_0 \approx 4 \text{ MeV}$ . The value of  $\bar{G}$  can be compared with the value  $G \approx 0.2 \text{ MeV}$  of the standard parametrization  $G = 25/A \text{ MeV}$ . It is seen from Fig. 10.1 that the pairing gap around the Fermi energy

Table 10.1. Matrix elements  $G_{\nu\nu'}$  of the induced interaction as shown in Fig. 10.2; The corresponding average value is  $\bar{G} = \sum_{\nu' \geq \nu} G_{\nu\nu'} / 15 = 0.11 \text{ MeV}$  (after Gori (2002)).

	$d_{5/2}$	$g_{7/2}$	$s_{1/2}$	$h_{11/2}$	$d_{3/2}$
$d_{5/2}$	0.08	0.016	0.182	0.158	0.109
$g_{7/2}$	0.016	0.08	0.05	0.022	0.143
$s_{1/2}$	0.182	0.05	0	0.124	0.272
$h_{11/2}$	0.158	0.022	0.124	0.179	0.032
$d_{3/2}$	0.109	0.143	0.272	0.032	0.167

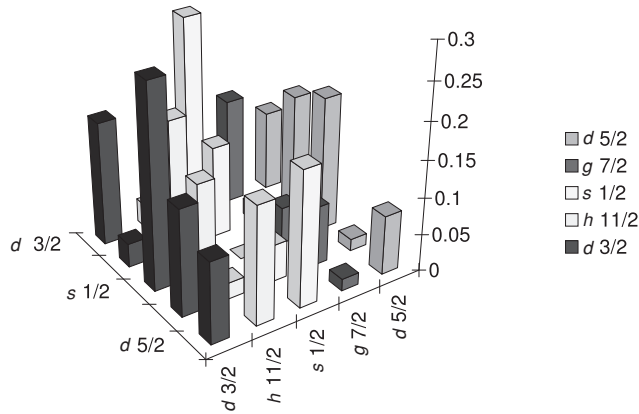


Figure 10.2. Matrix elements  $G_{\nu\nu'}$  of the induced interaction defined in equations (10.11)–(10.12) used in the calculation of the state-dependent pairing gap of  $^{120}\text{Sn}$  (equation (10.16)) shown in Fig.10.1 for levels lying close to the Fermi energy  $\varepsilon_F$  ( $\varepsilon_{d_{5/2}} = -12.0 \text{ MeV}$ ,  $\varepsilon_{g_{7/2}} = -10.9 \text{ MeV}$ ,  $\varepsilon_{s_{1/2}} = -9.7 \text{ MeV}$ ,  $\varepsilon_{h_{11/2}} = -9.21 \text{ MeV}$ ,  $\varepsilon_{d_{3/2}} = -9.0 \text{ MeV}$ ,  $\varepsilon_{f_{7/2}} = -4.0 \text{ MeV}$ ,  $\varepsilon_F = -9.2 \text{ MeV}$ ). The values on the ordinates are in MeV (after Gori (2002)).

is of the order of 0.8 MeV, which is an appreciable fraction of the empirical value of 1.4 MeV, obtained from the mass table (Audi and Wapstra (1995)) making use of the relation

$$\Delta = \frac{1}{2} [B(N - 2, Z) + B(N, Z) - 2B(N - 1, Z)], \tag{10.20}$$

where  $B(N, Z)$  is the binding energy of the nucleus with  $N$  neutrons and  $Z$  protons.

Fig. 10.3 shows the value of the state-dependent pairing gap averaged over levels lying in an energy interval of the order of  $\pm 2\Delta$  around the Fermi energy, for a number of Sn isotopes, in comparison with the corresponding empirical

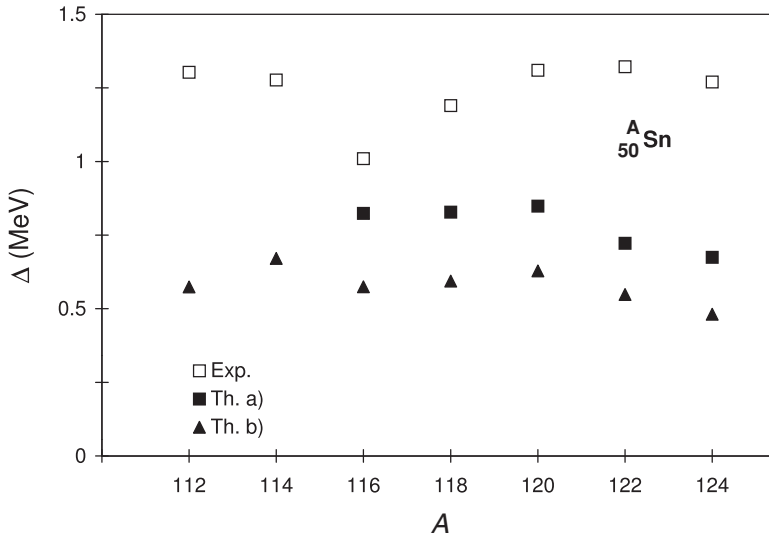


Figure 10.3. Average value of the state dependent pairing gap associated with levels lying close to the Fermi energy of  ${}_{50}^A\text{Sn}$  isotopes, calculated making use of the induced pairing interaction  $G_{\nu\nu'}$  (equations (10.11)–(10.12)), in comparison with the empirical pairing gap (see equation (10.20)). The results of two calculations are shown, associated with RPA solutions which fit two different sets of transition probabilities associated with the low-lying quadrupole and octupole surface vibrations. The first set (also used to obtain the results reported in Fig. 10.1) was taken from Beer *et al.* (1970), Th. a). The second set is from Jonsson *et al.* (1981), Th. b). Reprinted with permission from Barranco *et al.*, *Phys. Rev. Lett.* **83**:2147–50 (1999). Copyright 1999 by the American Physical Society.

values obtained from equation (10.20) and mass table. In all cases, theory accounts for a consistent fraction of the empirical values of the pairing gaps. If one were to reproduce this empirical value of  $\Delta$ , one would need to add to  $G_{\nu\nu'}$  an approximately constant quantity, which changes only slightly from isotope to isotope, and whose average value is  $G_0 \approx 0.06$  MeV. This corresponds to a parametrization  $G_0 = X/A$  MeV with  $X \approx 7$ .

The main contribution to the state-dependent pairing gap defined in equation (10.16) arises from the exchange of low-lying surface collective modes. In fact, repeating the calculation of  $\Delta_\nu$  but this time including only the lowest-lying surface vibrations ( $n = 1, \lambda^\pi = 2^+, 3^-, 4^+, 5^-$ ), one obtains results which coincide, within 20%, with those obtained from the full calculation. The main contributions arise from the exchange of low-lying quadrupole and octupole vibrations. These results are closely connected with the difference in matrix elements associated with low-lying collective surface vibrations and with giant resonances. In fact the average value of  $G_{\nu\nu'}$  resulting from the coupling to vibrational states with energy  $\hbar\omega_\lambda(n) \leq 7$  MeV is 0.08 MeV (see Fig. 10.4 and

Table 10.2. Induced matrix elements  $(G_{\nu\nu'})_{\text{low}}$  (in MeV) (see Fig. 10.4) (after Gori (2002)).

	$d_{5/2}$	$g_{7/2}$	$s_{1/2}$	$h_{11/2}$	$d_{3/2}$
$d_{5/2}$	0.059	0.01	0.156	0.124	0.07
$g_{7/2}$	0.01	0.062	0.028	0.015	0.12
$s_{1/2}$	0.156	0.028	0	0.074	0.258
$h_{11/2}$	0.124	0.015	0.074	0.162	0.02
$d_{3/2}$	0.07	0.12	0.258	0.02	0.162

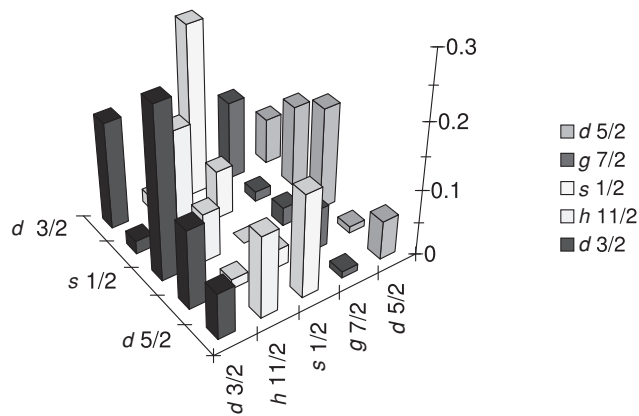


Figure 10.4. Induced interaction matrix elements  $(G_{\nu\nu'})_{\text{low}}$  (in MeV) associated with the exchange between nucleons moving in time-reversal states close to the Fermi energy  $\varepsilon_F$  of  $^{120}\text{Sn}$  of low-lying ( $\hbar\omega(n) \leq 7$  MeV) surface vibrations ( $\lambda^\pi = 2^+, 3^-, 4^+, 5^-$ ) (after Gori (2002)).

Table 10.2), while that associated with the coupling to vibrational states with  $\hbar\omega_\lambda(n) > 7$  MeV is 0.03 MeV (see Fig. 10.5 and Table 10.3). One expects that this small average value would become even smaller by considering the fact that giant resonances are not sharp states but display a damping width.

Because low-lying surface vibrations are built, to some extent, by the same valence nucleons which participate in the Cooper pair formation, one would expect that the values of  $(G_{\nu\nu'})_{\text{low}}$  shown in Fig. 10.4 (and thus the total value  $G_{\nu\nu'} = (G_{\nu\nu'})_{\text{low}} + (G_{\nu\nu'})_{\text{high}}$  shown in Fig. 10.2 as well as  $\Delta_\nu$  (Fig. 10.1) will be somewhat modified by Pauli principle corrections. In fact, it is found that these corrections modify (reduce), as a rule, the value of  $\Delta_\nu$  by about 10% from the value obtained by making use of equation (10.12) (Appendix F). This correction is expected to be larger in the case of light, halo nuclei (see next chapter).

Table 10.3. Matrix elements  $(G_{\nu\nu'})_{\text{high}}$  (in MeV) as shown in Fig. 10.5 (after Gori (2002)).

	$d_{5/2}$	$g_{7/2}$	$s_{1/2}$	$h_{11/2}$	$d_{3/2}$
$d_{5/2}$	0.026	0.007	0.04	0.044	0.048
$g_{7/2}$	0.007	0.025	0.025	0.009	0.036
$s_{1/2}$	0.04	0.025	0	0.064	0.046
$h_{11/2}$	0.044	0.009	0.064	0.042	0.016
$d_{3/2}$	0.048	0.036	0.046	0.016	0.027

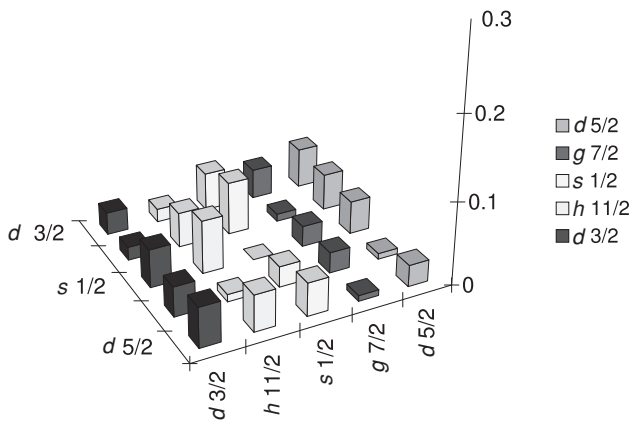


Figure 10.5. Induced matrix elements  $(G_{\nu\nu'})_{\text{high}}$  (in MeV) associated with the exchange of high-lying vibrations (essentially giant resonances) with  $\hbar\omega_{\lambda}(n) > 7$  MeV and  $(\lambda^{\pi} = 2^{+}, 3^{-}, 4^{+}$  and  $5^{-})$  between nucleons moving in time-reversal states close to the Fermi energy  $\varepsilon_{\text{F}}$  of  $^{120}\text{Sn}$  (after Gori (2002)).

In Fig. 10.6 the results of calculations of the pairing gap carried out as explained above for the isotopes  $^A\text{Ca}$  and  $^A\text{Ti}$  are shown compared with the empirical values obtained with the help of equation (10.20). The average value of  $G_{\nu\nu'}$  associated with levels lying close to the Fermi energy is, in this case, of the order of 0.2 MeV, while  $E_0$  is of the order of  $-3$  MeV. The induced interaction leads to pairing gaps which again, in these cases, account for a consistent fraction of the empirical value. The results furthermore display a similar dependence on  $A$  to that displayed by the experimental values, a dependence which reflects the shell dependence of the collective surface modes. In particular, the low predicted value of  $\Delta$  in  $^{50}\text{Ca}$  compared with  $^{42}\text{Ca}$  is due to the fact that the ‘core’  $^{48}\text{Ca}$  is more rigid than the core  $^{40}\text{Ca}$ , as can be seen from Fig. 10.7 where the  $\beta_2$  and  $\beta_3$  values associated with the different Ca-isotopes are reported.

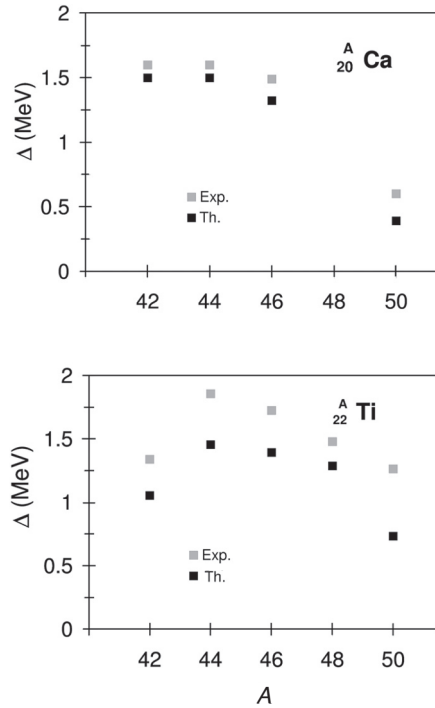


Figure 10.6. Average value of the state-dependent pairing gap associated with levels lying close to the Fermi energy of the  ${}^A\text{Ca}$ - and the  ${}^A\text{Ti}$ -isotopes, compared with the experimental data calculated by making use of the relation  $\Delta = \frac{1}{2}[B(N-2, Z) + B(N, Z) - 2B(N-1, Z)]$ , where  $B(N, Z)$  is the binding energy of the nucleus with  $N$  protons and  $Z$  neutrons, after Gori (2002).

Within this context it is interesting to note that the corresponding quantities for the Sn-isotopes are essentially constant as a function of  $A$  (see Fig. 10.8), a fact which is intimately connected with the essential constancy, as a function of  $A$ , observed in the gap of the Sn-isotopes (see Fig. 10.3).

The results discussed in this section may provide, at the microscopic level, insight into the success found by surface and density-dependent pairing interactions used in the literature to describe the low-energy nuclear structure (Green and Mozkowski (1965), Faessler (1968), Bertsch and Esbensen (1991)).

Let us conclude this section by noting that, because collective vibrations couple democratically to all nucleons, regardless of their isospin quantum number, the induced pairing-force mechanism is expected to lead to a consistent proton–neutron pairing correlation, as well as to multipole (in particular quadrupole) pairing correlations. Although the field has not been explored, calculations carried out in  ${}^{42}\text{Sc}$  (Barranco *et al.* (1999)) indicate this to be the case.

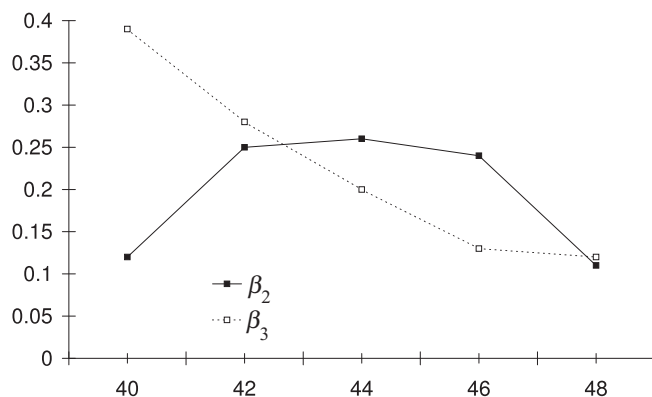


Figure 10.7. Value of the deformation parameters  $\beta_2$ ,  $\beta_3$  for the Ca-isotopes (after Gori (2002)).

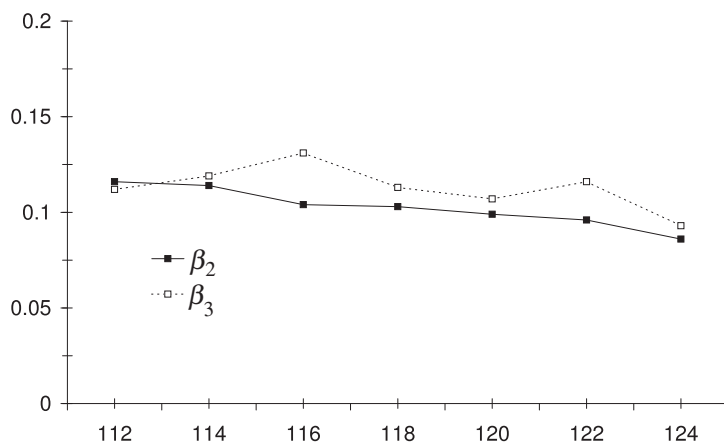


Figure 10.8. Value of the deformation parameters  $\beta_2$ ,  $\beta_3$  for the Sn-isotopes (Jonsson *et al.* (1981)) (after Gori (2002)).

### 10.3 Slab model

To assess the universality of the results presented in the previous section, we shall study the induced pairing interaction in a system free of shell effects, but retaining the properties associated with the confinement of nucleons by an elastic surface. For this purpose we use the slab model for semi-infinite nuclear matter proposed by Esbensen and Bertsch (1984a,b) and Bertsch and Esbensen (1985). In the present section the aim is to study the induced interaction between nucleons due to coupling with surface modes. The discussion here is based on the work of Giovanardi *et al.* (2002). The collective response of the nuclear surface is approximated by the RPA response function and the coupling of the nucleon motion to the surface vibrations is calculated self-consistently.

In the theory of Esbensen and Bertsch (1984a,b) the nucleons are confined in the half-space  $z < 0$  by the one-dimensional Fermi-like potential

$$V(z) = V_0(1 + e^{-z/a})^{-1}. \quad (10.21)$$

The single-particle wavefunctions in the potential (10.21) can be written as

$$\Phi_v(\vec{r}) = e^{i\vec{k}_{vp} \cdot \vec{r}_p} \phi_v(z). \quad (10.22)$$

The corresponding energy eigenvalues and momentum parallel to the surface are  $\varepsilon_v = \frac{\hbar^2 k_{vp}^2}{2m} + \varepsilon_{vz}$  where  $\vec{k}_{vp} = (k_{vx}, k_{vy}, 0)$ . The vector  $\vec{r}_p$  is parallel to the plane of the surface of the slab ( $x, y, 0$ ). The wavefunctions  $\phi_v(z)$  are solutions of the single-particle Schrödinger equation

$$\left( \frac{-\hbar^2}{2m} \frac{d^2}{dz^2} + V(z) \right) \phi_v(z) = \varepsilon_{vz} \phi_v(z), \quad (10.23)$$

normalized so that, for  $z \rightarrow -\infty$ ,

$$\phi_v(z) = \sqrt{2} \cos(k_{vz}z + \theta_v), \quad (10.24)$$

where  $k_{vz}$  is the asymptotic wavenumber and  $\theta_v$  a phase.

The next step in the calculation of the induced interaction consists in determining the vibrational modes of the system. For this purpose one diagonalizes the surface-peaked separable interaction

$$v(\vec{r}, \vec{r}') = k_0 g(|\vec{r}_p - \vec{r}'_p|) V'(z) V'(z'), \quad (10.25)$$

in a particle-hole basis and in the harmonic approximation (RPA). The quantity  $V'(z)$  is the derivative of the potential defined in equation (10.21). The finite-range Yukawa interaction acting in the  $x, y$ -direction,

$$g(|\vec{r}_p - \vec{r}'_p|) = \frac{e^{|\vec{r}_p - \vec{r}'_p|/a_r}}{2\pi a_r |\vec{r}_p - \vec{r}'_p|}, \quad (10.26)$$

with  $a_r = 1$  fm, has been chosen so as to give a realistic value of the nuclear surface tension (1 MeV/fm<sup>2</sup>). The coupling strength  $\kappa_0$  is determined by the relation

$$\kappa_0^{-1} = \int dz \rho'_0(z) V'(z), \quad (10.27)$$

which expresses the self-consistent condition existing between density and potential fluctuations associated with the normal modes. Diagonalizing the interaction given in equation (10.26) in the harmonic approximation (RPA) one can construct the linear response function

$$R^{\text{RPA}}(K, \hbar\omega) = \frac{R^0(K, \hbar\omega)}{1 - \kappa_0 \tilde{g}(K) R^0(K, \hbar\omega)}. \quad (10.28)$$

It is written in terms of the unperturbed response  $R^0(K, \hbar\omega)$  which, in the slab model, can be accurately parametrized by an oscillator response function

$$R^0(K, \hbar\omega) = \frac{N}{\hbar} \left( \frac{1}{(\omega - \omega_0) + i\gamma/2} - \frac{1}{(\omega + \omega_0) + i\gamma/2} \right). \quad (10.29)$$

The energy centroid  $\hbar\omega_0(K)$ , the width  $\hbar\gamma(K)$  and normalization strength  $N(K)$  are functions of  $K$ . The function

$$\tilde{g}(K) = \frac{1}{\sqrt{1 + (a_r K)^2}} \quad (10.30)$$

is the kernel of the two-dimensional Fourier transform

$$g(|\vec{r}_p - \vec{r}'_p|) = \int \frac{d^2K}{(2\pi)^2} e^{i\vec{K}(\vec{r}_p - \vec{r}'_p)} \tilde{g}(K).$$

The unperturbed strength function is proportional to the imaginary part of  $R^0(K, \hbar\omega)$ ,

$$S_0(K, \hbar\omega) = -\frac{1}{\pi} \text{Im} R^0(K, \hbar\omega). \quad (10.31)$$

It is a symmetric function of  $K$  and is antisymmetric in  $\omega$ .

The RPA strength function is an even function of  $K$  and an odd function of  $\omega$ . It can be expressed in terms of the unperturbed response as

$$S^{\text{RPA}}(K, \hbar\omega) = \left( \frac{S_0(K, \hbar\omega)}{(1 + \kappa \text{Re} R^0(K, \hbar\omega))^2 + (\kappa\pi S_0(K, \hbar\omega))^2} \right), \quad (10.32)$$

where  $\kappa(K) = \kappa_0 \tilde{g}(K)$ . Esbensen and Bertsch showed that the denominator in equation (10.32) vanishes when  $\omega = 0$  and  $K = 0$  because of the self-consistency condition (10.27). When  $\omega$  and  $K$  are small

$$S^{\text{RPA}}(K, \hbar\omega) \propto \frac{\omega}{\omega^2 + \alpha K^2}, \quad (10.33)$$

where  $\alpha$  depends on the parameters in  $S_0$  and  $\tilde{g}(K)$ .

Now we consider the process in which pairs of nucleons moving in time-reversal states exchange the eigenmodes of equation (10.28). We shall denote by  $k_{v_p}$  and  $k_{v'_p}$  the momentum of the single-particle states in the initial and in the final channels respectively, in a plane parallel to that of the surface while  $k_{v_z}$  and  $k_{v'_z}$  denote the asymptotic momentum along the  $z$ -direction. The wavenumber  $\vec{K}$  of the exchanged phonon is fixed by the relation expressing the parallel momentum conservation, i.e.

$$\vec{K} = \vec{k}_{v_p} - \vec{k}_{v'_p}.$$

The equation corresponding to (10.12) for the induced pairing matrix element in the microscopic calculation in Section 12.2 can be written as

$$G_{\nu\nu'}(K) = 2(\kappa_0 \tilde{g}(K))^2 M_{\nu\nu'}^2 \times \int_0^\infty d\hbar\omega \frac{S^{\text{RPA}}(K, \hbar\omega)}{E_0 - (|e_\nu| + |e_{\nu'}| + \hbar\omega)}. \quad (10.34)$$

The single-particle energies are defined by  $e_j \equiv \varepsilon_j - \varepsilon_F$  ( $j = \nu, \nu'$ ), where  $\varepsilon_F$  is the Fermi energy while

$$\varepsilon_\nu \equiv \varepsilon_{\nu p} + \varepsilon_{\nu z} = \frac{\hbar^2 k_{\nu p}^2}{2m} + \varepsilon_{\nu z}, \quad (10.35)$$

$$\varepsilon_{\nu'} \equiv \varepsilon_{\nu' p} + \varepsilon_{\nu' z} = \frac{\hbar^2}{2m} (\vec{k}_{\nu p} - \vec{K})^2 + \varepsilon_{\nu' z}. \quad (10.36)$$

The surface interaction matrix element is

$$M_{\nu\nu'} = \int dz \phi_{k_{\nu'z}}^*(z) V'(z) \phi_{k_{\nu z}}(z). \quad (10.37)$$

and  $E_0$  is the pair-correlation energy. Equation (10.34) has the same Bloch–Horowitz energy denomination as the induced pairing interaction in Section 10.2.

The total number of particles in the slab is

$$A = 2V \int \frac{d^3k}{(2\pi)^3} V^2(\vec{k}), \quad (10.38)$$

where  $V$  is the volume of the system. It is related to the surface area  $S$  and the thickness  $d$  of the slab by

$$V = S \cdot d.$$

This relation can be used to make a connection with finite nuclei. Putting  $V = \frac{4}{3}\pi R^3$  and  $S = 4\pi R^2$  in the surface area, one obtains

$$d = 0.4 A^{1/3}. \quad (10.39)$$

In the framework of Bloch–Horowitz perturbation theory, the BCS number and gap equations

$$N = 2V \int \frac{d^2k}{(2\pi)^3} V^2(k), \quad (10.40)$$

$$\Delta(\vec{k}_\nu) = 2d^{-1} \int \frac{d^3k_{\nu'}}{(2\pi)^3} \frac{G_{\nu\nu'}(K)}{2} U(\vec{k}_{\nu'}) V(\vec{k}_{\nu'}) \quad (10.41)$$

are solved self-consistently. The induced pairing matrix element  $G_{\nu\nu'}(K)$  diverges when  $K = 0$  because of the  $1/\omega$  singularity in the unperturbed strength function. The approximation (10.33) for  $S^{\text{RPA}}$  which holds for small values of

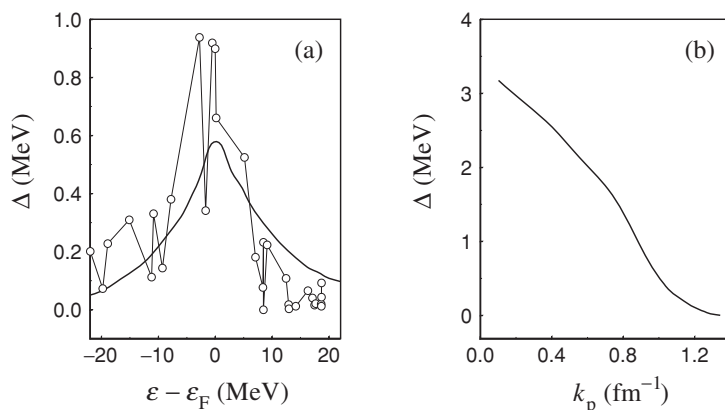


Figure 10.9. (a) Pairing gap of particles as a function of the particle energy  $\varepsilon - \varepsilon_F = (\hbar k_v)^2/(2m) - \varepsilon_F$ , for  $R = 6$  fm. For each energy value, the pairing gap  $\Delta$  has been calculated as an average over the gaps of particles having the same  $k_v^2$ . Detailed results for the nucleus  $^{120}\text{Sn}$  are also shown (open dots, see Fig. 10.1). (b) The pairing gap of a particle at the Fermi energy as a function of the momentum component parallel to the surface of the slab. The gap goes to zero when  $(k_v)_p = 1.337 \text{ fm}^{-1}$ , corresponding to the case of particles moving in a plane parallel to the surface of the slab ( $k_z = 0$ ). Reprinted with permission from Giovanardi *et al.*, *Phys. Rev.* **C65**: 041304 (R) (2002). Copyright 2002 by the American Physical Society.

$\omega$  and  $K$  shows that  $G_{\nu\nu'}(K)$  diverges as  $\ln|K|$  for small  $K$ . Because this divergence is only logarithmic the integral in the gap equation converges. Equation (10.31) shows that  $g(K) = 1$  for a zero-range interaction ( $a_r = 0$ ) and that  $g(K) \propto 1/(a_r K)^2$  for large  $K$  for a finite range interaction. Hence, because of the factor  $g(K)$  in equation (10.34), the finite-range Yukawa interaction suppresses the high  $K$  contributions to  $G_{\nu\nu'}(K)$ . This corresponds to the high multipolarity surface vibrations in finite nuclei.

In the remainder of this section we discuss numerical results obtained by Giovanardi *et al.* (2002). They take the depth of the potential in equation (10.21) to be  $V_0 = -45$  MeV with a diffusivity  $a = 0.75$  fm. Because of the finite thickness of the slab the pairing gap  $\Delta(\vec{k}_v)$  is not an isotropic function of  $\vec{k}_v$ . An energy-dependent pairing gap can be defined by averaging  $\Delta(\vec{k}_v)$  over all the single-particle states with the same single-particle energy. This state-dependent pairing gap is shown in Fig. 10.9(a) as a function of  $\varepsilon - \varepsilon_F = (\hbar k_v)^2/(2m) - \varepsilon_F$  for  $R = 6$  fm ( $A \approx 120$ ). The results for the nucleus  $^{120}\text{Sn}$  from Section 10.2 are also shown (see Fig. 10.1). As expected, the pairing gap peaks at the Fermi surface, the associated FWHM reflecting the frequency distribution of the linear response of the system. In Fig. 10.9(b) we display the pairing gap associated with a particle at the Fermi energy as a function of the momentum component  $k_v$  lying in the  $(x, y)$ -plane parallel to the surface of the slab. The marked decrease

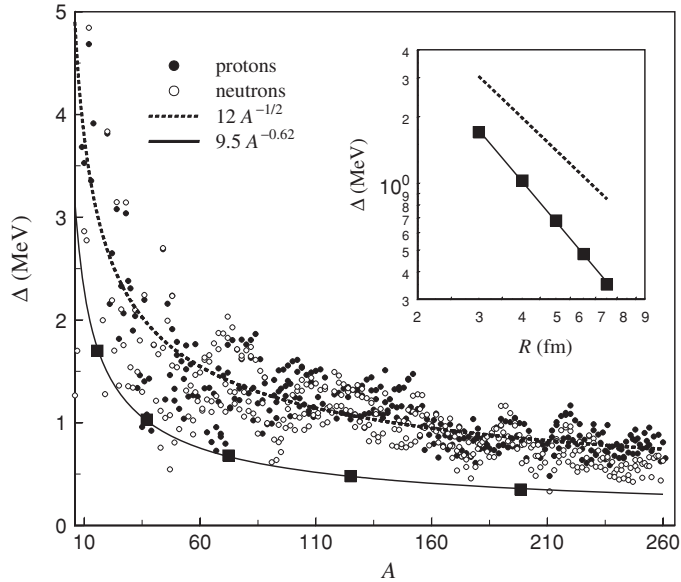


Figure 10.10. The experimental pairing gap of neutrons (open dots) and protons (solid dots) as a function of the mass number  $A$ , calculated from the nuclear binding energies (see equation (10.20)) are described, on average, by the function  $12A^{-1/2}$  MeV (dotted curve) (Bohr and Mottelson (1969)). The solid squares show the results of the self-consistent solution of equations (10.34)–(10.41), results which are well fitted by the expression  $\Delta = 9.5A^{-0.62}$  MeV. In the inset, the same results are displayed as a function of the nuclear radius  $R$  in a log-log scale, to emphasize the different behaviour of the two power laws. Reprinted with permission from Giovanardi *et al.*, *Phys. Rev. C* **65**: 041304 (R) (2002). Copyright 2002 by the American Physical Society.

of  $\Delta$  as a function of  $k_v$  testifies to the surface origin of the induced pairing interaction  $G_{v\nu'}$  (equation (10.34)).

Following equations (10.41) and (10.40) the pairing gap should scale according to  $A^{-1/3}$ . This is, however, altered by the averaging and by the discrete spectrum of energies  $\varepsilon_{v_z}$  associated with motion in the  $z$ -direction.

In Fig. 10.10 we show the pairing gap  $\Delta_{\text{slab}}$ , obtained by solving equations (10.34)–(10.41), and averaging  $\Delta(k_v)$  over single-particle states with energy  $|\varepsilon_v - \varepsilon_F| \leq 4$  MeV. The results are well fitted by the power law

$$\Delta_{\text{slab}} \approx \frac{9.5}{A^{0.62}} \text{ MeV}, \quad (10.42)$$

where the exponent of the mass number  $A$  is quite close to  $2/3$ , typical of surface phenomena. In keeping with the fact that the experimental values are reproduced, on average, by the standard expression given in equation (1.30), i.e.

$$\Delta_{\text{exp}} \approx 12/\sqrt{A}, \quad (10.43)$$

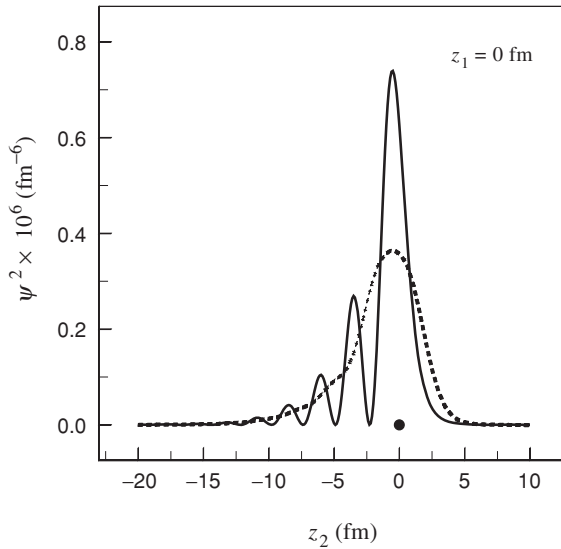


Figure 10.11. Plot of  $\psi^2$  (equation (10.44)), for  $R = 6$  fm and for particles with zero relative parallel coordinate ( $R_p = 0$ ), obtained fixing the coordinate of one particle ( $z_1$ , solid dot), as a function of the coordinate of the second particle ( $z_2$ ). The surface of the slab is located at  $z = 0$ . Also shown is the value of  $\psi^2$  averaged over an interval of  $\approx 5$  fm (dashed curve). Reprinted with permission from Giovanardi *et al.*, *Phys. Rev.* **C65**: 041304 (R) (2002). Copyright 2002 by the American Physical Society.

one concludes that  $\Delta_{\text{slab}} \approx (0.45 \pm 0.04)\Delta_{\text{exp}}$ . In other words, the induced pairing interaction leads to pairing gaps which are of the order of 50% of those experimentally observed, a result which is similar to that obtained in the case of detailed calculations in finite nuclei.

To account for the experimental pairing gap, one needs to add to the interaction  $G_{\nu\nu'}$  an extra contribution which we shall parametrize as  $G_0/A$ . One finds that  $G_0 \approx (0.4 \pm 0.1)G$ , where  $G/A$  is the strength of the pairing interaction which reproduces the experimental data (see Fig. 10.10, dotted curve). In particular, in the case of  $R = 7$  fm, i.e.  $A = 200$ , one obtains  $G = 27$  MeV, while  $G_0 = 17$  MeV.

The results shown in Figs. 10.11 and 10.12 provide further insight into the role that the surface of a confined Fermi liquid has in the formation of Cooper pairs. In Fig. 10.11, the modulus squared of the anomalous density (closely connected with the Cooper pair wavefunction)

$$\begin{aligned} \psi(z_1, z_2, R_p) = & \int \frac{dk_p}{2\pi} k_p J_0(k_p R_p) \int \frac{dk_z}{2\pi} \phi_{k_z}(z_1) \phi_{k_z}(z_2) \\ & \times U(k_p, k_z) V(k_p, k_z), \end{aligned} \quad (10.44)$$

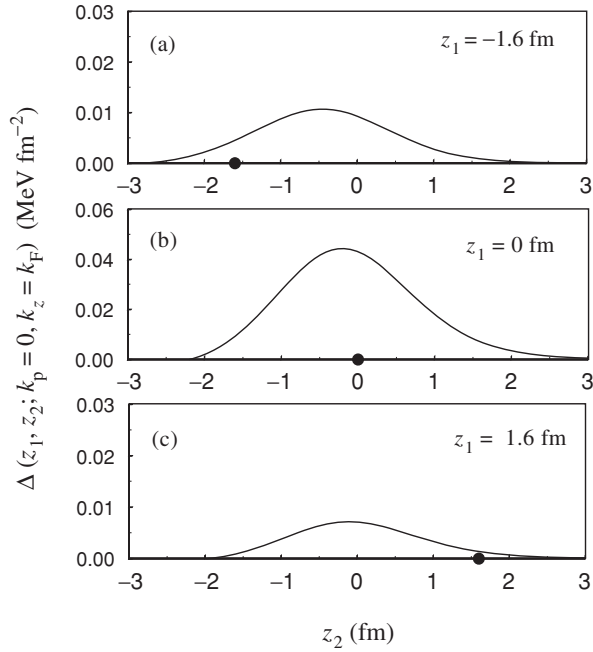


Figure 10.12. Pairing gap calculated, for  $R = 6$  fm, as the product of the anomalous density  $\psi$  (equation (10.44)) and the induced interaction  $v$  (equation (10.45)), as a function of the  $z$ -coordinate of one of the two particles ( $z_2$ ), giving the coordinate of the other particle ( $z_1$ ) fixed values. Reprinted with permission from Giovanardi *et al.*, *Phys. Rev.* **C69**: 041304 (R) (2002). Copyright 2002 by the American Physical Society.

is shown as a function of the coordinate  $z_2$  of one of the particles, fixing the coordinate  $z_1 (= 0)$  of the other particle on the surface. In the above equation,  $J_0$  is a Bessel function and  $R_p$  is the distance between particles in the direction parallel to the surface of the slab. Making use of the function  $\psi$  we have calculated the mean square radius  $\langle r^2 \rangle^{1/2} = (\int d^3r r^2 |\psi|^2 / \int d^3r |\psi|^2)^{1/2}$  of the Cooper pair, obtaining 22 fm. This quantity is closely connected with the coherence length  $\xi = \hbar v_F / \pi \Delta$  of the pair. Because  $\varepsilon_F \approx 36$  MeV and  $\Delta \approx 0.6$  MeV at the Fermi energy, one obtains, from this simple estimate,  $\xi = 28$  fm.

The pairing gap  $\Delta(z_1, z_2, R_p) = G_{v v'}(z_1, z_2, R_p) \times \psi(z_1, z_2, R_p)$  is obtained by multiplying the anomalous density by the induced interaction, defined in equation (10.34), a quantity which depends on  $e_v$  and  $e_{v'}$ . For single-particle levels lying close to the Fermi energy we can neglect this dependence and write

$$G(z_1, z_2, R_p) = 2 \int \frac{d^2 K}{2\pi^2} k_0^2 \tilde{g}(K) \frac{V'(z_1) V'(z_2)}{d^2} e^{iK R_p} \times \int d\hbar\omega \frac{\text{Im} R^{\text{RPA}}(K, \omega)}{E_0 - \hbar\omega}. \quad (10.45)$$

In Fig. 10.12, the Fourier transform  $\Delta(z_1, z_2, k_p)$  of the quantity  $\Delta(z_1, z_2, R_p)$ , in a plane parallel to the surface, and setting  $k_p = 0$ , is shown as a function of the  $z_2$ -coordinate of one of the two particles, and the other coordinate  $z_1$  is given a fixed value. As expected, the probability that the two partners of a Cooper pair are close together, and thus that the associated pairing gap is large, is higher at the surface of the slab than elsewhere.

#### 10.4 Induced pairing interaction, effective mass and vertex correction processes

As discussed in Section 9.3 there is an intimate relation between the self-energy process renormalizing the mass of the nucleons ( $\omega$ -mass) and the pairing gap arising from Cooper pair formation through the exchange of surface vibrations between nucleons moving in time-reversal states close to the Fermi surface. In the above calculations the  $\omega$ -dependence of the effective mass has been neglected. While this approximation is the same as that employed in the standard treatment of pairing leading to BCS number and gap equations (see Chapter 3), its range of validity is an open question. This is because setting  $m^* = m$  implies that the occupation probability of the single-particle states is either 1 ( $\varepsilon_v \leq \varepsilon_F$ ) or 0 ( $\varepsilon_v > \varepsilon_F$ ). Consequently, they can fully participate in the processes leading to pair formation and thus to nuclear superfluidity. On the other hand, in the case in which  $m^* = \frac{m_\omega m_k}{m} \approx m$ , although apparently identical to the previous one, the spectroscopic factor associated with single-particle states lying close to the Fermi energy is  $Z_\omega \approx (m_\omega/m)^{-1}$  (see equation (9.23)). Because  $m_\omega/m > 1$ ,  $Z_\omega < 1$ , implying that the nucleons spend part of their time in more complicated configurations, configurations which make use also of empty states within the independent-particle approximation leading to an effective reduction of the space available to the particles to correlate ( $\Omega_{\text{eff}} < \Omega$ ). Consequently, these single-particle states can participate less effectively in producing the nuclear condensate, a handicap which is further accentuated by taking into account the splitting of the single-particle strength (see equation (9.41) and Section H.4).

##### 10.4.1 Solution of the Dyson equation for normal and abnormal densities

Barranco *et al.* (2004) have investigated these questions in the case of a typical superfluid nucleus, i.e.  $^{120}\text{Sn}$ . The formalism used is based on the Dyson equation (Terasaki *et al.* (2002a,b), Van der Sluys *et al.* (1993)). It gives a consistent description of the dressed, single-particle state  $\tilde{a}$  of an odd nucleon renormalized by the (collective) response of all the other nucleons (Figs. 10.13(a)–10.13(d)), the renormalization of the energy  $\hbar\omega_v$  (Figs. 10.14(a)–10.14(b)) and of the transition probability  $B(E\lambda)$  (Figs. 10.14(c)–10.14(f)) of the collective vibrations of the even system (correlated particle–hole excitations), and the induced interaction

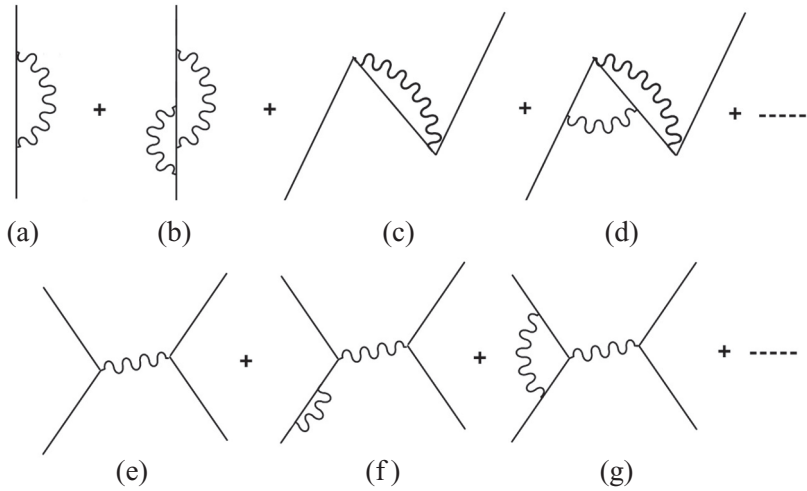


Figure 10.13. Renormalization processes arising from the particle-vibration coupling phenomenon. A line indicates quasiparticles obtained from BCS theory, making use of the mean-field single-particle states of the Skyrme parametrization Sly4 and the nucleon–nucleon  $v_{14}$  Argonne potential. The wavy line indicates the vibrational states (after Broglia *et al.* (2004)).

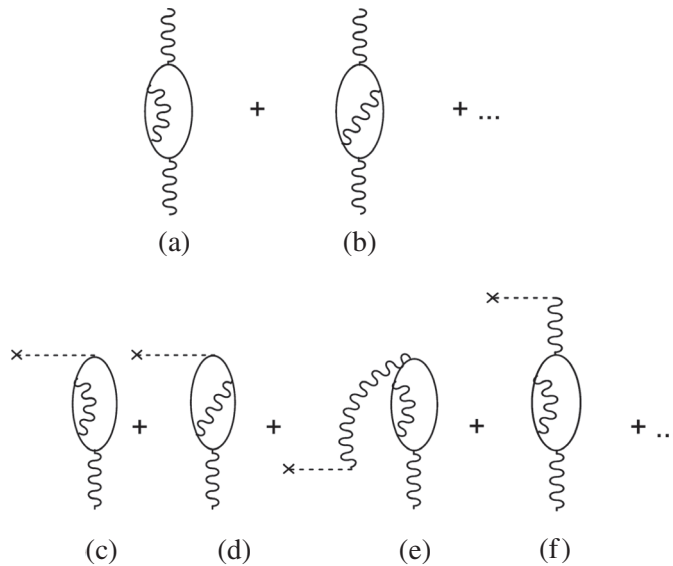


Figure 10.14. Most relevant processes taken into account in the renormalization of the energy of the phonon (a,b) and of the associated transition strength (c–f).

due to the exchange of collective vibrations between pairs of nucleons, moving in time-reversal states close to the Fermi energy (Figs. 10.13(e)–10.13(g)). It includes both self-energy and vertex correction processes. Within this framework, the self-consistency existing between the dynamical deformations of the density and of the potential sustained by ‘screened’ particle-vibration coupling vertices leads to renormalization effects which stabilize the collectivity and the self-interaction of the elementary modes of nuclear excitation, in particular of the low-lying surface vibrational modes. This procedure produces a rather accurate description of experimental findings, in terms of very few parameters, namely: the  $k$ -mass  $m_k$  (equations (8.19) and (8.17)) and the particle-vibration coupling vertex  $V(j, j' : \lambda)$  (see equation (8.31)).

A Skyrme interaction (Sly4 parametrization, with  $m_k \approx 0.7m$ ) was used to determine the properties of the bare single-particle states, while the resulting particles were allowed to interact through the Argonne  $V_{14}$  nucleon–nucleon interaction, as well as to exchange phonons.

As seen from Fig. 10.15, Hartree–Fock theory is not able to account for the experimental quasiparticle energies of the low-lying states. Diagonalizing the

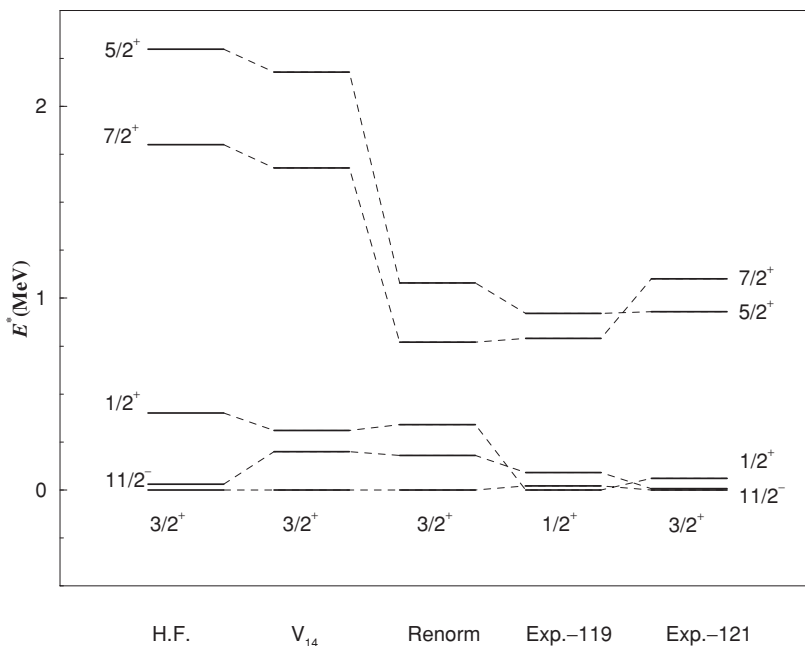


Figure 10.15. The spectra of the lowest quasiparticle states in  $^{120}\text{Sn}$  calculated using Hartree–Fock theory, BCS with the Argonne  $V_{14}$  potential, and after renormalization, are compared with the experimental levels in the odd neighbouring nuclei  $^{119}\text{Sn}$  and  $^{121}\text{Sn}$  (after Barranco *et al.* (2004)).

Table 10.4. The energy and reduced E2 transition strength of the low-lying  $2^+$  state, calculated according to different theoretical models, are compared to the experimental values (Stelson et al. (1970)) (after Barranco et al. (2004)).

	$\hbar\omega_{2^+}$ (MeV)	B(E2 $\uparrow$ ) ( $e^2 \text{ fm}^4$ )
RPA (Gogny)	2.9	660
RPA (Sly4)	1.5	890
RPA + renorm	0.9	2150
Exp.	1.2	2030

Argonne  $V_{14}$  nucleon–nucleon potential in the Hartree–Fock basis, within the framework of the BCS approximation including scattering states up to 800 MeV above the Fermi energy (to achieve convergence, repulsive core) in a spherical box of radius equal to 15 fm, one obtains the state-dependent pairing gap shown in Fig. 8.9 (labelled  $V_{14}$ ). The resulting pairing gap (average value for levels around the Fermi energy) accounts for about half of the empirical pairing gap value ( $\approx 1.4$  MeV) obtained from the odd–even mass difference. In keeping with this result, the quasiparticle spectrum (see Fig. 10.15), although being slightly closer to the experimental findings than that predicted by Hartree–Fock theory, displays large discrepancies with observations. The situation is rather similar concerning the low-lying quadrupole vibration of  $^{120}\text{Sn}$  calculated in the QRPA with standard effective nucleon–nucleon interactions like Gogny or Skyrme forces. While energy is predicted too high, which may not be very important, the B(E2) value is too small by about a factor of 3 (see Table 10.4), a result which calls for a better theory.

In fact, renormalizing the energy and the transition strength of the  $2^+$  phonon, i.e. considering couplings of the type depicted in Fig. 10.14, couplings which have been shown to be essential in determining, for example, the width of giant resonances (see Fig. 8.16), one obtains an increase of the B(E2) transition probability which brings theory essentially in agreement with experiment (see Table 10.4). The most important processes which renormalize the energy of the phonon are shown in Figs. 10.14(a) and (b). Other graphs which are also of fourth order in the particle–vibration coupling vertex, but contain intermediate states with more than four quasiparticle states, lead to very small contributions. This is because these terms not only involve larger denominators, but also, because of their higher degree of complexity, give rise to contributions with ‘random’ phases which tend to cancel each other. This is a consequence of the fact that, while cancellation between the contribution associated with graphs (a) and (b) of Fig. 10.14 is strong in the particle–hole channel, the opposite is

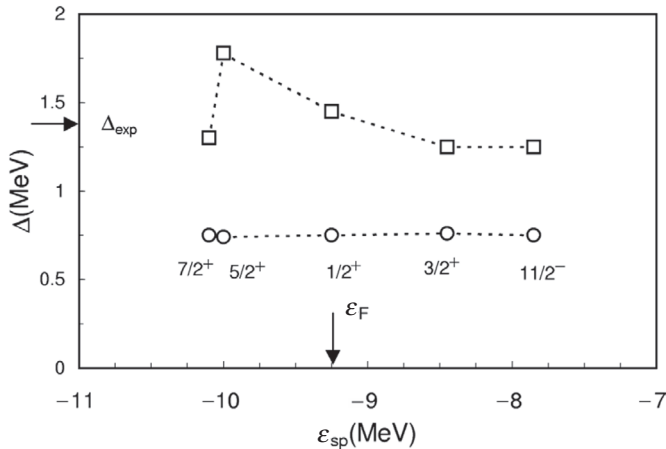


Figure 10.16. The state-dependent pairing gap for the levels close to the Fermi energy obtained using BCS theory with the  $\nu_{14}$  Argonne potential (circles) is compared with the result obtained by also including renormalization effects (squares) (after Barranco *et al.* (2004)).

true in the particle–particle channel (see equations (A.49) and (A.50)), and that the phonons are calculated in a Bogoliubov–Valatin-quasiparticle basis. In keeping with the above discussion, the most important processes renormalizing the  $B(E2)$  transition probability are those shown in Figs. 10.14(c),(d),(e) and (f).

Solving the Dyson equation by making use of phonons which account for the experimental findings, the state-dependent pairing gap shown in Fig. 10.16 was obtained. The average value of the resulting state-dependent pairing gap of  $^{120}\text{Sn}$  is now close to the value  $\Delta_{\text{exp}} = 1.4 \text{ MeV}$  derived from the odd–even mass difference. In Fig. 10.15 the energy centroid of the peaks carrying the largest quasiparticle strength are shown, for the orbitals around the Fermi energy. These results provide an overall account of the lowest quasiparticle states measured in the odd systems  $^{119}\text{Sn}$  and  $^{121}\text{Sn}$ . In the case of  $d_{5/2}$  orbital, the associated quasiparticle strength is strongly fragmented, and displays three low-energy peaks which collect less than 40% of the single-particle strength. Figures 10.15 and 10.16 show, respectively, the energy and the pairing gap associated with the lowest of these three peaks.

The results discussed in this section seem to be in contradiction with the results discussed in connection with Figs. 8.6 and 8.9. In fact, from these two figures one could expect that essentially the full effect associated with the increase of the pairing gap arising from the polarization processes, examples of which are shown in Fig. 10.13, are associated with effective mass processes like those displayed in Fig. 10.13(a) (see also equation (8.21)), leaving a negligible role to induced interaction processes like those shown in Fig. 10.13(e). The resolution of such an apparent contradiction is to be found in the fact that effective mass

processes simultaneously renormalize the density of levels  $N(0)$  and the pairing interaction  $G$ . However, while  $(N(0))_{\text{dressed}} \sim N(0)/Z_\omega$ ,  $(G)_{\text{dressed}} \sim Z_\omega^2 G$ , the overall effect being  $(GN(0))_{\text{dressed}} \sim Z_\omega(GN(0))$ . Because  $Z_\omega < 1$ , effective mass effects lead to a decrease of the pairing gap, decrease which is corrected to the value to be compared to the experimental data, by the contribution  $Z_\omega^2 v_{\nu\nu'}$  arising from the induced interaction (see equation (9.33)). In fact, a further decrease of  $N(0)$  is associated with fragmentation of the single-particle strength arising from renormalization processes like the one shown in Fig. 10.13(a) and measured by the (state dependent) width  $\Gamma(j, \omega)$  (see Sections 9.1.2 and 9.3, equation (9.41)).

For a detailed account of these effects we refer to Morel and Nozières (1962), Schrieffer (1964), Mahan (1981) and Baldo *et al.* (2002). Also to Combescot (1999). A simple estimate of the relative importance of the different processes is given in Appendix H (Section H.4).

### 10.5 Superfluidity in the inner crust of neutron stars

There exists considerable experimental evidence which testifies to the fact that pulsars are rotating neutron stars (Pines *et al.* (1992)). It is believed that the crust of a neutron star is, in its outer part ( $10^6 \text{ g cm}^{-3} < \rho < 10^{11} \text{ g cm}^{-3}$  and a few hundred metres thick), made out of nuclei arranged in a Coulomb lattice and of a nearly homogeneous background of relativistic electrons. As one goes deeper into the crust, because of the rising electron Fermi energy, the nuclear species become progressively more neutron-rich, beginning as  $^{56}\text{Fe}$  and going through  $^{118}\text{Kr}$  at mass density  $\rho_d = 4.3 \times 10^{11} \text{ g cm}^{-3}$ , at which point neutrons are barely bound (Negele and Vautherin (1973)). At this density, known as the ‘neutron drip density’, nuclei have become so neutron-rich that, with increasing density, the neutron states lying in the continuum begin to be filled and the lattice of neutron-rich nuclei becomes permeated by a sea of free neutrons.

The region of densities  $\rho_d < \rho < 0.7\rho_0$  (where  $\rho_0 = 0.17$  nucleons per  $\text{fm}^3 \approx 3 \times 10^{14} \text{ g cm}^{-3}$  corresponds to saturation density, and where  $\rho_d = 4.3 \times 10^{11} \text{ g cm}^{-3}$  is the ‘neutron drip’ density) is the so-called ‘inner crust’ (thickness about one kilometre), where a Coulomb lattice of neutron-rich nuclei is permeated by a sea of free neutrons. In keeping with the fact that the nuclear interaction is, in this range of densities, attractive for pairs of nucleons moving in time-reversal states ( $^1S_0$  neutron–neutron scattering, see Fig. 8.1) and because of the relatively low temperatures ( $\leq 0.1 \text{ MeV}$ ) associated with all but the youngest of neutron stars, the free neutrons are believed to pair and form an isotropic s-wave superfluid. A proper understanding of the superfluidity properties of neutron-rich nuclei embedded in a sea of free neutrons (Wigner–Seitz cell) is of importance to determine the thermal properties of the neutron star crust, which is expected to play a central role in the early stages ( $\approx 10^2$  years since formation) of the cooling

of neutron stars (Yakovlev and Pethick (2004), Pizzochero *et al.* (2002)). This knowledge is also important for the understanding of the vortex motion in the neutron superfluid within the solid crust of the neutron star, believed to be the origin of observed sudden decrease of the rotational period (spinup), or glitches (see Fig. 6.2) observed, for example, in the Crab ( $|\Delta P|/P \approx 10^{-8}$ ) and Vela ( $|\Delta P|/P \approx 2 \times 10^{-6}$ ) pulsar periods  $P$  (Alpar (1977), (1998), Anderson and Itoh (1975), Epstein and Baym (1988), Link and Epstein (1991), Pizzochero *et al.* (1997), Donati and Pizzochero (2003)).

Much effort has been concentrated in describing superfluidity of a uniform neutron star system using realistic nucleon–nucleon interactions (see e.g. Kennedy (1968), Sauls (1989), Takahara *et al.* (1994), Chen *et al.* (1986), Takatsuka (1984), Baldo *et al.* (1990), (1991), Chen *et al.* (1993), Wambach *et al.* (1993), Delion *et al.* (1995), Schulze *et al.* (1996), Lombardo and Schulze (2001), and references therein). However, in all the calculations, the role of impurities represented by nuclei in the sea of free neutrons has been neglected. In keeping with the fact that the pairing gap depends strongly on baryon density, a proper treatment of superfluidity in the neutron star crust should take into account the simultaneous presence of the free neutrons as well as the neutrons bound in the atomic nuclei (see also Delion *et al.* (1995)). To this purpose, theory should be able to provide, making use of a realistic interaction, equally reliable results for the uniform infinite system, as for the isolated atomic nucleus, limiting situations in which the results can be compared with a variety of calculations and with experimental data respectively. A unified description of these limiting situations will lend confidence to the results associated with finite atomic nuclei embedded in a sea of free neutrons. Contributions to carry out this programme are found in Barranco *et al.* (1997) and Gori *et al.* (2004b) (see also Sandulescu *et al.* (2004)).

The quantum mechanical calculations of the pairing gap in the inner crust of neutron stars were carried out by solving the Hartree–Fock–Bogoliubov (HFB) equations (see Barranco *et al.* (1997), Barranco *et al.* (1998) and Section 8.1.1 equations (8.4)–(8.6); see also Dobaczewski *et al.* (2002), Dobaczewski and Nazarewicz (1998)).

In Barranco *et al.* (1997) the single-particle states  $|a_k\rangle = |n_k(l_a 1/2)j_a m_a\rangle$  describing the motion of nucleons in the mean fields calculated by Negele and Vautherin (1973) for each Wigner–Seitz cell density with a nucleus at the centre, and parametrized in terms of a Saxon–Woods potential, are labelled by the quantum numbers specifying the number of nodes  $n_k$ , the orbital angular momentum  $l_a$ , the total angular momentum  $j_a$  and its third component  $m_a$ , as well as the parity  $(-1)^{l_a}$ . The states  $|\tilde{a}_1\rangle$  are obtained from the original states by the operation of time reversal. The quantities  $U_{a_k}^i$  and  $V_{a_k}^i$  are the occupation amplitudes of the single-particle states while  $E_i$  is the quasiparticle energy. The Argonne  $v_{14}$  potential was used in the calculation of the matrix elements

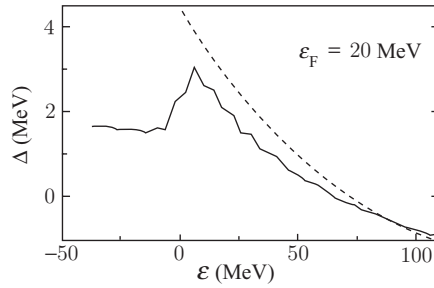


Figure 10.17. The pairing gaps obtained in a Wigner–Seitz cell of radius equal to 15 fm, and  $\varepsilon_F = 20$  MeV, containing the nucleus Sn whose bound states are described in terms of a Saxon–Woods potential with a radius of 6.26 fm and a depth of 45.5 MeV, are shown by a solid and dashed curve, respectively for a diffusivity  $a = 0.67$  fm and  $a = 0$  fm. The gaps obtained for the discrete states have been averaged over 4 MeV. The gaps obtained for uniform neutron matter are shown by the dashed line (from Barranco *et al.* (1997)). Reprinted from *Physics Letters B*, Vol. 390, Barranco *et al.*, ‘Role of finite nuclei on the pairing gap of the inner crust of neutron stars’, page 15, Copyright 1997, with permission from Elsevier.

$\langle a_1 \tilde{a}_2 | v | b_1 \tilde{b}_2 \rangle$  (see Section 8.1). The quantity  $\varepsilon_F$  is the Fermi energy of the system and thus determines the average number of nucleons. To obtain convergence of the HFB equations, single-particle states lying as high as 600 MeV have to be included in the calculations. To this purpose the continuum is discretized by placing the nucleus in a box. For  $\varepsilon_F > 0$ , the radius of the box  $R_{\text{box}}$  coincides with the Wigner–Seitz cell radius  $R_{\text{WS}}$  as calculated by Negele and Vautherin (1973). For  $\varepsilon_F < 0$ ,  $R_{\text{box}}$  should be varied until convergence of the results is achieved.

A number of situations corresponding to the densities discussed in this reference have been worked out. Particularly illustrative is the system composed of a nucleus containing 50 protons placed in the centre of a Wigner–Seitz cell of radius  $R_{\text{WS}} = 15$  fm. Setting the Fermi energy at  $\varepsilon_F = 20$  MeV ( $\rho = 0.18\rho_0$ ), the Wigner–Seitz cell contains 600 neutrons. That is, we can view the system as a gigantic neutron-rich nucleus  ${}_{50}^{600}\text{Sn}$ . The selected density leads to the largest value of the pairing gap at the Fermi energy for the system under discussion (see Fig. 10.18).

Note that the large value of the pairing gap obtained in this calculation is connected with the fact that the single-particle energies were determined by making use of the bare nucleon mass and not the  $k$ -mass (see in this connection Figs. 8.6 and 8.9 as well as Sections 8.2 and 10.4). The same comment applies to Fig. 10.17, in which we display the diagonal part of the neutron pairing gap  $\Delta_{a_k}$  ( $\equiv \Delta_{a_k a_k}$ ) associated with the single-particle states of the system, obtained by solving equations (8.4)–(8.6) with  $\varepsilon_F = 20$  MeV. The results have been averaged over an energy interval of 4 MeV to smooth out fluctuations associated with particular shells. The quantity  $\Delta_{a_k}$  has a peak that corresponds to single-particle levels just barely unbound ( $\varepsilon_{a_1} \approx 0$  MeV). It decreases as  $\varepsilon_{a_1}$  increases,

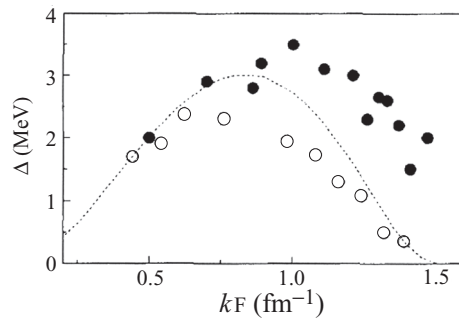


Figure 10.18. The dashed curve shows the pairing gaps at the Fermi energy in neutron matter as a function of the Fermi momentum. The solid dots show the pairing gaps of bound levels close to the Fermi energy, for different negative Fermi energies in the Saxon–Woods potential (with  $a = 0.65$  fm) used in connection with Fig. 8.6 to describe  $^{120}\text{Sn}$ . The Fermi momentum is referred to the bottom of the well. The open dots show the pairing gaps of levels close to the Fermi energy for positive values of  $\varepsilon_F$  and for the Wigner-Seitz cell discussed in connection with Fig. 10.17. Reprinted from *Physics Letters B*, Vol. 390, Barranco *et al.*, ‘Role of finite nuclei on the pairing gap of the inner crust of neutron stars’, page 15, Copyright 1997, with permission from Elsevier.

in keeping with the fact that the content of relative momentum associated with such configurations also increases (see e.g. Baldo *et al.* (1990)). The pairing gap also decreases for bound neutron levels, because the density inside the nucleus is higher than outside it. The fact that the pairing gap does not vanish for bound levels ( $\varepsilon_{a_1} < 0$ ), i.e. levels inside the nucleus, highlights the role the nuclear surface plays in the pairing phenomenon in atomic nuclei. We also show in Fig. 10.17 the pairing gap  $\Delta(k)$  associated with uniform neutron matter as a function of the energy  $\varepsilon = \hbar^2 k^2 / 2m$ , calculated again setting  $\varepsilon_F = 20$  MeV. From these calculations one concludes that the presence of the nucleus in the sea of free neutrons leads to an overall reduction of the pairing gap in the energy range  $0 < \varepsilon < 100$  MeV, and the appearance of a broad bump near the edge of the single-particle potential well.

Results of calculations of the pairing gap for uniform neutron matter as a function of neutron Fermi wavenumber  $k_{F_n}$  (as a measure of density) for six models of crustal superfluidity are shown in Fig. 10.19 (from Lombardo and Schulze (2001)). The model labelled BCS is the simplest in which the pairing interaction is taken to be the neutron–neutron interaction in free space (see also Fig. 10.18). The five others – C86 (Chen *et al.* (1986)), C93 (Chen *et al.* (1993)), A (Ainsworth *et al.* (1989)), W (Wambach *et al.* (1993)), and S (Schulze *et al.* (1996)) include medium polarization effects which weaken the pairing. While all curves exhibit the same qualitative behaviour, there are also important differences. The BCS model is oversimplified, since it does not take into account effects of the medium.

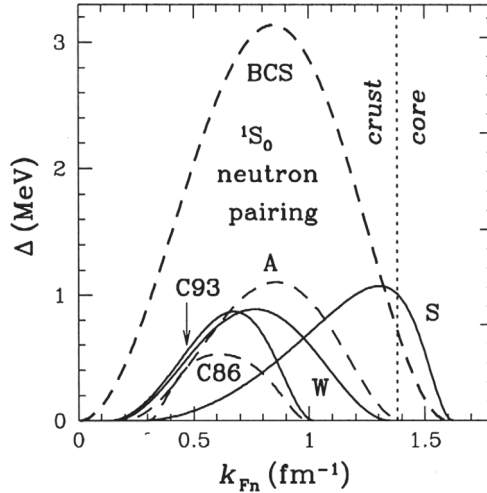


Figure 10.19. Energy gaps (left vertical axis) for various models of crustal neutron pairing as a function of neutron Fermi wavenumber. The vertical dotted line marks the crust–core interface (after Lombardo and Schulze (2001)).

Concerning the other results, one observes large variations in the predictions for the upper density at which neutron superfluidity disappears. While the reason for these differences is unclear, that the neglect of pairing fluctuations, fluctuations which become quite important when the mean-field pairing gap goes to zero, is likely to be one of the causes (see Section 6.6, Fig. 6.24).

In an infinite (3D) medium (i.e. a system where  $r_s \ll \xi \ll L$  see Section 4.1.1, equation (4.1) and subsequent discussion) the gap is affected mainly by exchange of spin fluctuations, which reduce fluctuations, just as they do in metals. This is very different from what is found in the case of a finite (0D) medium ( $r_s < L \ll \xi$ ), where density modes have a dominant role. The difference in the relative role played by density and magnetic modes in 0D and 3D systems is at the basis of the fact that medium polarization enhances the pairing gap in finite nuclei while it quenches it in the inner crust of neutron stars (see e.g. Figs. 10.16 and 10.19). This point is taken up in the next section.

### 10.5.1 Interplay between density and magnetic modes

In this section we discuss the mechanism which is at the basis of the seemingly contradictory results, namely the fact that while medium effects increase the nuclear pairing gap, they reduce it in the case of the inner crust of neutron stars. We shall show that these results are a natural consequence of the different (relative) collectivity displayed by density  $S = 0$  (mainly surface) and  $S = 1$  spin (mainly volume) modes in (infinite) neutron matter and in (finite) atomic nuclei

(Gori *et al.* (2004b), see also Schrieffer (1994), Gor'kov and Melik-Barkhudrov (1961), Bortignon *et al.* (1983)). Strictly speaking, in the case of atomic nuclei, spin is not a good quantum number with which to identify the polarization quanta, because of the strong spin-orbit term present in these systems. We have thus adopted the criterion of distinguishing between natural ( $\pi = (-1)^J$ ) and non-natural ( $\pi = -(-1)^J$ ) parity modes, where  $J$  indicates the total angular momentum of the quanta. The classification reduces to that of  $S = 0$  and  $S = 1$  modes in the limit of no spin-orbit interaction.

In the following we address the question on hand within the scenario provided by the paradigmatic (superfluid) open-shell nucleus  $^{120}\text{Sn}$ . The starting point corresponds to the calculation of the mean-field potential and associated quasiparticle properties within the framework of Hartree–Fock plus BCS theory using the SkM\* force (Bartel *et al.* (1982)). The polarization quanta were worked out within the framework of quasiparticle random phase approximation (QRPA) (see e.g. Coló and Bortignon (2001)) making use of the particle–hole interaction

$$\begin{aligned} v_{\text{ph}}(\vec{r}, \vec{r}') &= \frac{\delta^2 E_{\text{HF}}}{\delta\rho(\vec{r})\delta\rho(\vec{r}')} & (10.46) \\ &= \{[F_0 + F'_0\vec{\tau} \cdot \vec{\tau}'] + [(G_0 + G'_0\vec{\tau} \cdot \vec{\tau}')\vec{\sigma} \cdot \vec{\sigma}']\} \delta(\vec{r} - \vec{r}'). \end{aligned}$$

In what follows we shall only consider the diagonal part of the  $\vec{\tau} \cdot \vec{\tau}$  terms, in keeping with the fact that we are here interested in the neutron–neutron pairing interaction. Off-diagonal terms are associated with charge-exchange modes. Thus, in lowest order, they do not contribute to the neutron–neutron interaction, but are expected to be of relevance in the discussion of the proton–neutron pairing interaction.

The functions  $F_0(\vec{r})$ ,  $F'_0(\vec{r})$ ,  $G_0(\vec{r})$  and  $G'_0(\vec{r})$  (see also Section 4.3, discussion following equation (4.80)), generalized Landau–Migdal (Landau (1959), Migdal (1967)) parameters controlling the isoscalar and isovector (spin-independent and spin-dependent) channels are displayed in Fig. 10.20.

Vibrations of multipolarity  $J = 2, 3, 4$  and 5 of both natural and unnatural parity were worked out. Those having energy  $\leq 30$  MeV were used in the calculation of the induced interaction (see Fig. 10.21(a)). The associated transition densities are

$$\begin{aligned} \delta\rho_\alpha^i(r) &= \frac{1}{\sqrt{2J+1}} \sum_{1,2} (X_{1,2}(i, \alpha) + \beta Y_{1,2}(i, \alpha)) \\ &\quad \times (U_1 V_2 - c U_2 V_1) \times \langle j_1 || \hat{O}_\alpha || j_2 \rangle \varphi_1(r) \varphi_2(r), \end{aligned} \quad (10.47)$$

where one can have  $\alpha = J$ ,  $\beta = +1$ ,  $\hat{O}_\alpha = Y_J$  or  $\alpha = JL$ ,  $\beta = -1$ ,  $\hat{O}_\alpha = [Y_L \times \sigma]_J$  (concerning  $c$ , see Eq. (3.89)). The index  $i$  labels the different vibrational modes of a given spin and parity in order of increasing energy, while  $X$  and  $Y$  are the forwardsgoing and backwardsgoing QRPA amplitudes of the corresponding modes.

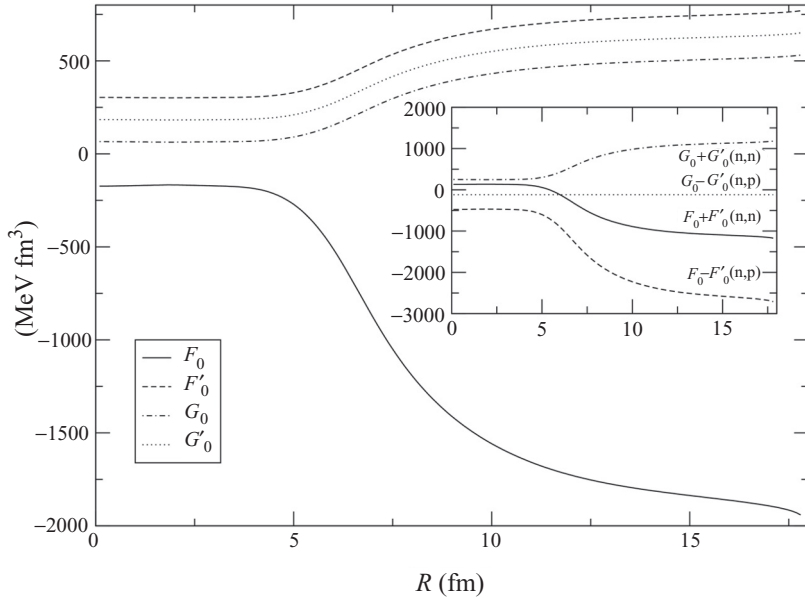


Figure 10.20. Generalized Landau parameters associated with the interaction SkM\* defining the strength of the particle-hole interaction in the isoscalar ( $F_0$ ), isovector ( $F'_0$ ), spin isoscalar ( $G_0$ ) and spin isovector ( $G'_0$ ) channels. In the inset the functions  $F_0 + F'_0$  (n-n interaction),  $F_0 - F'_0$  (n-p),  $G_0 + G'_0$  (n-n) and  $G_0 - G'_0$  (n-p) are also shown. After Gori *et al.* (2004b).

We now calculate the induced pairing matrix elements associated with the exchange of polarization quanta between pairs of neutrons moving in time-reversed states. For this purpose the particle (neutron)-vibration coupling matrix elements are worked out:

(a) spin independent

$$\begin{aligned} & \langle j'm', JM | [F_0(r) + F'_0(r)\vec{\tau} \cdot \vec{\tau}'] \delta(\vec{r} - \vec{r}') | jm \rangle \\ & \sim \int dr \varphi_{j'} [(F_0 + F'_0)\delta\rho_{Jn}^i + (F_0 - F'_0)\delta\rho_{Jp}^i] \varphi_j, \end{aligned} \quad (10.48)$$

$\delta\rho_{Jn}^i$  and  $\delta\rho_{Jp}^i$  being the neutron and proton contributions to the transition densities defined in equation (10.47),

(b) spin dependent

$$\begin{aligned} & \langle j'm', JM | [G_0(r) + G'_0(r)\vec{\tau} \cdot \vec{\tau}'] \vec{\sigma} \cdot \vec{\sigma}' \delta(\vec{r} - \vec{r}') | jm \rangle \\ & \sim \int dr \varphi_{j'} [(G_0 + G'_0)\delta\rho_{JLn}^i + (G_0 - G'_0)\delta\rho_{JLp}^i] \varphi_j. \end{aligned} \quad (10.49)$$

These particle-vibration coupling matrix elements, together with the energies of the modes and the HF single-particle energies are the basic ingredients needed to

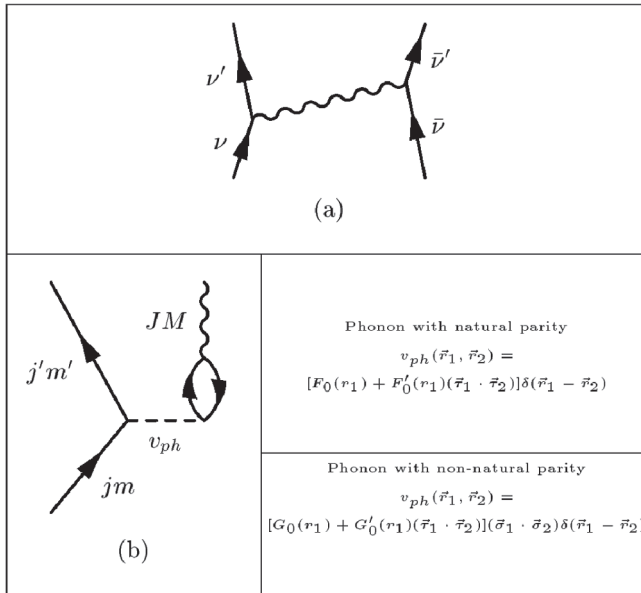


Figure 10.21. (a) Diagram depicting the pairing interaction induced by the exchange of phonons; (b) particle-vibration coupling vertex making explicit the dominant part of the particle-hole interaction giving rise, through the sum of bubble diagrams, to the corresponding QRPA modes (wavy line).

calculate the pairing induced interaction  $v_{\text{ind}}$  (see Fig. 10.21(a)). For non-natural parity modes, only the matrix elements (10.49) contribute. For natural parity modes, the matrix elements (10.48) are the dominant ones, and one can show that they are the only ones contributing to the diagonal matrix elements, which are displayed in Fig. 10.22. In this case it is thus possible to distinguish between the contributions associated with the exchange of  $S = 0$  (density) and  $S = 1$  (spin) vibrations. From Fig. 10.22 we can see that the exchange of spin fluctuations gives rise to repulsive matrix elements, while the exchange of density fluctuations leads to attractive matrix elements, the net result being predominantly attractive (in any case around the Fermi energy).

The resulting state-dependent pairing gap obtained by solving the BCS gap and number equations making use of the (total) induced pairing matrix elements ( $S = 0$  (density) plus  $S = 1$  (spin) modes) is depicted in Fig. 10.23(a). For states close to the Fermi energy they account for a consistent fraction of the experimental value (1.4 MeV). If one solves the BCS equations considering only the exchange of density modes (i.e. neglecting the contributions from equation (10.49)), one obtains values which are, on average, larger (see Fig. 10.23(b)). In fact, the exchange of  $S = 1$  modes quenches the pairing gap arising from the exchange of only  $S = 0$  modes by roughly 30%.

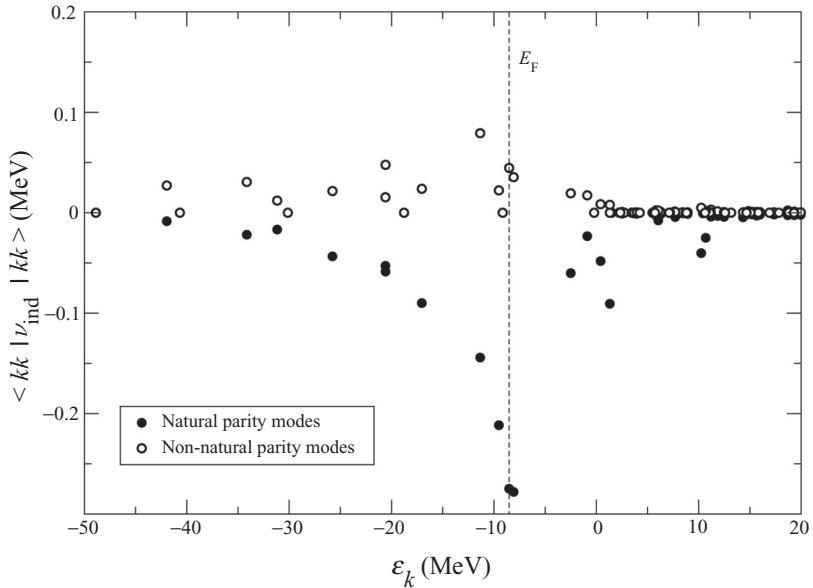


Figure 10.22. Diagonal induced pairing matrix elements resulting from the exchange of phonons with natural parity (solid circles) and those resulting from the exchange of phonons with non-natural parity vibrations (open circles), displayed as a function of the energy of the single-particle state  $\epsilon_k$ . Note that the induced matrix elements in this figure can be directly compared with the empirical constant  $G = 25/A (\approx 0.2 \text{ MeV}, A = 120)$  used to describe pairing correlations in nuclei within the framework of the BCS theory and a (pairing) force of constant matrix elements (after Gori *et al.* (2004b)).

To gain insight into what one would expect from these results in the case of infinite systems, we study the radial dependence of the particle-vibration coupling vertices shown in Fig. 10.21(b). The  $S = 0$  modes associated with induced pairing matrix elements have a clear surface character. In particular, this is the case for the most attractive pairing matrix element which is associated with the  $1h_{11/2}^2(0)$  ( $\epsilon_{1h_{11/2}} = -8.07 \text{ MeV}$ ,  $\epsilon_F = -8.50 \text{ MeV}$ ) configuration (see Fig. 10.22). Because of its large centrifugal barrier, the wavefunction of this single-particle state is mainly concentrated at the nuclear surface. The main contribution to the corresponding induced pairing matrix element arises from the exchange of a  $2^+$  phonon (of energy 1.5 MeV) between the two nucleons moving in time-reversal states in the  $h_{11/2}$  orbital. The associated proton and neutron transition densities depicted in Fig. 10.24(a) testify to the fact that this phonon has the character of a surface vibration. Concerning the most repulsive matrix elements, we have found that the corresponding  $S = 1$  phonons are volume modes. In particular, the largest (positive) matrix element is associated with the  $2d_{3/2}^2(0)$  configuration ( $\epsilon_{2d_{3/2}} = -8.52 \text{ MeV}$ ). Because of the low angular momentum, one

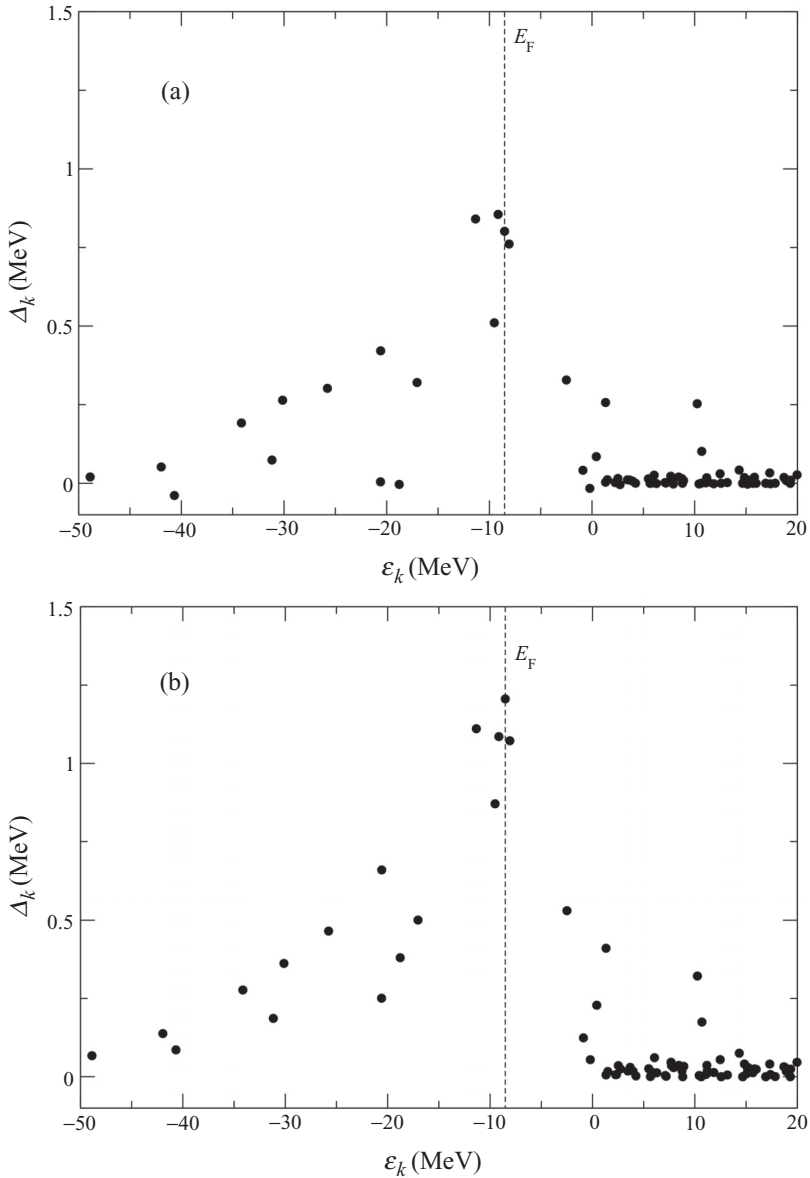


Figure 10.23. (a) The state-dependent pairing gap as a function of the single-particle energies obtained by solving the BCS equations associated with the total ( $S = 0$ ) + ( $S = 1$ ) induced interaction matrix elements; (b) same as (a) but for the induced interaction matrix elements produced only by exchange of density modes ( $S = 0$ ) (after Gori *et al.* (2004b)).

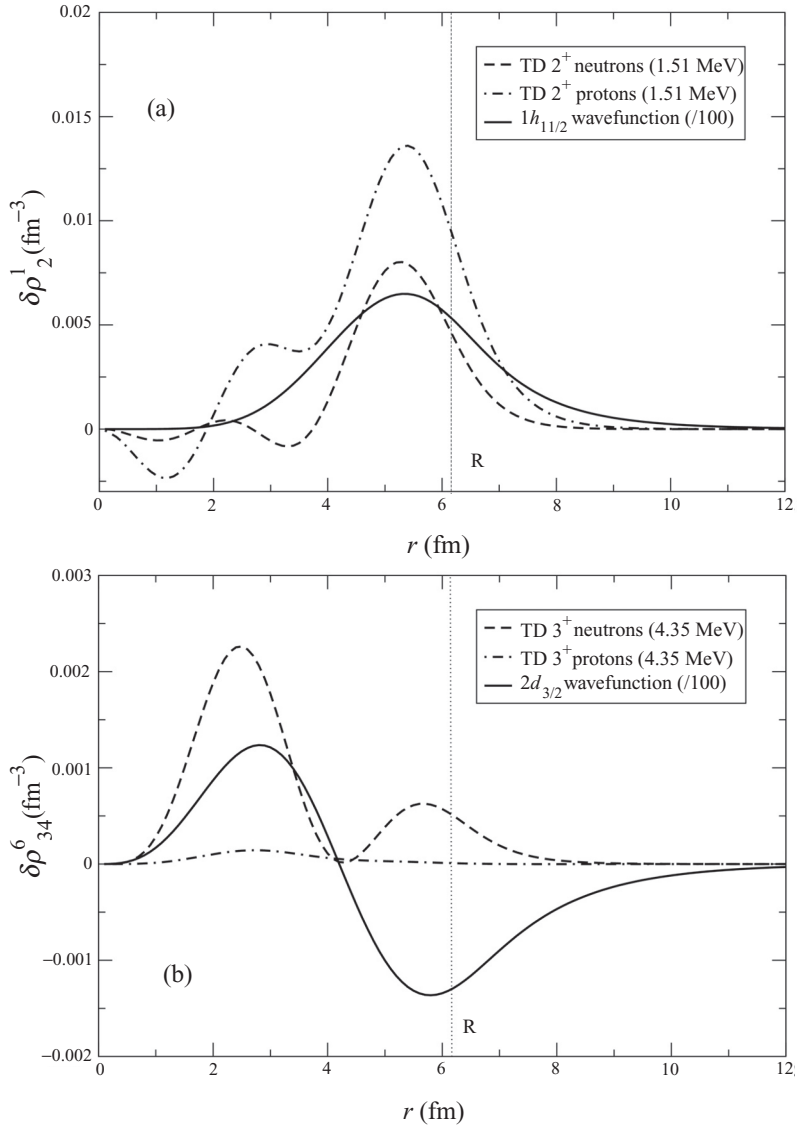


Figure 10.24. (a) The dashed and dot-dashed curves are respectively the neutron and proton transition densities associated with the  $2^+$  phonon with energy 1.5 MeV while the solid curve is the wavefunction of the  $1h_{11/2}$  state (in arbitrary units). (b) The same as (a) but for the  $3^+$  phonon with energy 4.35 MeV and the  $2d_{3/2}$  state (after Gori *et al.* (2004b)).

finds that a consistent fraction of the corresponding wavefunction is concentrated in the interior of the nucleus. This state can thus couple efficiently with phonons of volume character. In fact, the major contribution to the corresponding matrix element is due to the exchange of the  $3^+$  vibration (with energy at 4.35 MeV)

which is a mode with a large volume component as testified by the corresponding proton and neutron transition densities shown in Fig. 10.24(b). One can conclude that states lying close to the Fermi energy with high  $j$  and thus localized at the surface mainly feel the (attractive) coupling arising from the exchange of  $S = 0$  phonons. Because the contributions of these states to the gap equation are larger (statistically) than those associated with low- $l$  states (lying also close to the Fermi energy), the resulting induced pairing interaction in nuclei is attractive. The situation is expected to be quite different in the case of infinite neutron matter. In fact, in going from the finite to the infinite system the collectivity of the  $S = 0$ , mainly surface modes will be strongly reduced, while not much is expected to happen to the  $S = 1$ , mainly volume modes.

Furthermore, in going from nuclear ( $N = Z$ ) to neutron matter ( $N = A$ ), many attractive contributions vanish. In fact, if we turn off the neutron–proton interaction contributing to the basic vertices shown in Fig. 10.20, a strongly net repulsive induced interaction is obtained (see Fig. 10.25), a situation which much resembles the neutron star case. This result can be understood by realizing that, while the function  $F_0 + F'_0$  (corresponding to the particle–phonon coupling mediated by  $\delta\rho_{Jn}^i$ ) has a node at the nuclear surface (see inset to Fig. 10.20),

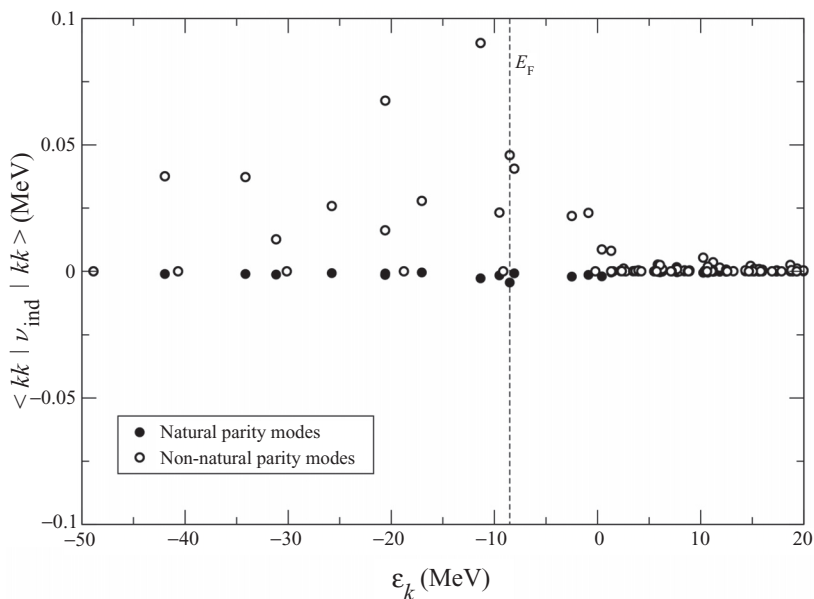


Figure 10.25. The diagonal matrix elements produced by the exchange of phonons with natural parity (filled circles) and those produced by the exchange of phonons with non-natural parity (empty circles) when the proton part of the phonon wavefunction is not included in the calculation, are displayed as a function of the energy of the single-particle state  $\epsilon_k$  (after Gori *et al.* (2004b)).

$G_0 + G'_0$  (corresponding to the particle-phonon coupling mediated by  $\delta\rho_{JLn}^i$ ) is large and positive.

Summing up, the exchange of low-lying vibrations (in which neutrons and protons participate on equal footing) between pairs of nucleons moving in time-reversal states close to the Fermi energy leads to a sizeable attractive pairing interaction which accounts for about 70% of the pairing gap. The inclusion of spin (volume) modes, reduces that contribution by 30% in the case of finite nuclei, bringing the induced pairing contribution to the pairing gap to a value of the order of  $\approx 50\%$ , the other half coming from the bare nucleon–nucleon force. Spin modes overwhelm density modes when the coupling to surface (namely  $S = 0$ ) modes as well as the proton–neutron coupling are neglected, a situation which mimics neutron matter.